Journal of Volcanology and Geothermal Research 461 (2025) 108276

Contents lists available at ScienceDirect

Journal of Volcanology and Geothermal Research

journal homepage: www.journals.elsevier.com/journal-of-volcanology-and-geothermal-research

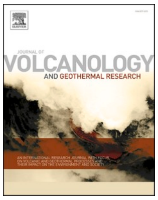

A review of the differential scanning calorimetry shift–factor approach: Application to Colli Albani melt viscosity and implications for mafic Plinian eruptions

E. Fanesi [a], D. Di Genova [b,*], P. Valdivia [b,c], D. Bondar [b,c], S. Dominijanni [d], S. Abeykoon [a], G. Giuliani [e], A. Kurnosov [c], G. Giordano [e], M. Cassetta [f], A. Vona [e], C. Romano [e], F. Arzilli [a]

[a] *School of Science and Technology, Geology Division, University of Camerino, Camerino, Italy*
[b] *Institute of Science, Technology and Sustainability for Ceramics (ISSMC) of the National Research Council (CNR), Via Granarolo 64, I–48018 Faenza, RA, Italy*
[c] *Bayerisches Geoinstitut, University of Bayreuth, Universitätsstraße 30, 95447 Bayreuth, Germany*
[d] *Institute of Environmental Geology and Geoengineering, CNR, Via Salaria Km 29.300, Rome 00015, Monterotondo, Italy*
[e] *Dipartimento di Scienze, Università degli Studi Roma Tre, Largo San L. Murialdo 1, 00146 Rome, Italy*
[f] *Department of Earth Sciences, University of Turin, Via Valperga Caluso, 35, 10125 Turin, Italy*

ARTICLE INFO

Keywords:
Viscosity
DSC
Phonotephrite
Nanolite
Colli Albani

ABSTRACT

The differential scanning calorimetry (DSC) shift factor has recently been applied to model the viscosity of volcanic melts, revealing that such melts are often less viscous and more prone to nanoscale phase separation and crystallization of nanolites (i.e., nanostructuration) than previously thought.

In this study, we investigate the melt viscosity and structural evolution of the tephri–phonolite "Pozzolane Nere" (PNR) magma from the Colli Albani volcanic district (Rome, Italy), which fed one of the largest Plinian eruptions of this volcanic system. By combining viscometry, conventional and flash DSC, and spectroscopic techniques – Raman, Mössbauer, and Brillouin – we examine the melt viscosity and structure both under anhydrous and hydrous conditions.

Our results demonstrate that the PNR melt is highly susceptible to nanocrystallization, particularly during viscometry, leading to a significant increase in viscosity compared to previous estimates. Additionally, the data suggest that under pre–eruptive conditions (1050 °C and $H_2O = 5$ wt%), the melt exhibits a viscosity one log unit lower than predicted by models. Upon dehydration, the viscosity increases remarkably, by up to 4300–fold. These findings imply that the low–viscosity behavior of PNR melt at depth could facilitate rapid magma storage and transfer through deep transcrustal magma pathways, supporting the rapid ascent needed for explosive mafic eruptions. Our results also imply that, despite this lower viscosity, the strong tendency of the PNR melt towards nanostructuration is likely to play a critical role in influencing magma rheology, as well as degassing and outgassing processes in the conduit.

These findings provide new insights into the magma storage and ascent dynamics, shedding light on how these processes may facilitate relatively rapid accumulation of mafic magmas in shallow reservoirs prior to highly explosive eruptions driven by rapid and significant crystallization.

1. Introduction

Magmas are typically stored and transported in sub-liquidus environments, where they behave as complex two- or three-phase suspensions of melt, crystals, and gas bubbles. This multiphase nature influences magma rheology significantly, as the temperature- and chemical-dependent structure of the melt, along with the presence of crystals and bubbles, can dramatically affect flow behavior during storage and ascent. Understanding these physicochemical multiphase interactions is crucial for unraveling magma dynamics in realistic geological scenarios (Kolzenburg et al., 2022).

Of particular interest here is the melt phase within the magma, as its structure and viscosity play a pivotal role in dictating volcanic eruption dynamics (Dingwell, 1996). For over fifty years, Earth and material

---

* Corresponding author.
E-mail address: danilo.digenova@cnr.it (D. Di Genova).

https://doi.org/10.1016/j.jvolgeores.2025.108276
Received 16 November 2024; Received in revised form 18 January 2025; Accepted 19 January 2025

scientists have been investigating the structural characteristics of melts, measuring their viscosity, and developing empirical models to predict their behavior under volcanic conditions (Bottinga and Weill, 1972; Giordano et al., 2008a; Hess and Dingwell, 1996; Hui and Zhang, 2007; Langhammer et al., 2022; Mysen et al., 1985, 1980; Romine and Whittington, 2015; Shaw, 1972; Stebbins et al., 1984).

Despite these advances, recent findings have uncovered a crucial, previously unrecognized phenomenon – supercooled volcanic melts are highly susceptible to rapid nanostructuration, resulting in crystallization within timescales that are typical for ambient pressure viscosity measurements (Bondar et al., 2025; Di Genova et al., 2017a, 2020a; Kleest et al., 2020; Liebske et al., 2003; Okumura et al., 2022a; Scarani et al., 2022a; Valdivia et al., 2024, 2023; Verdurme et al., 2023; Vetere et al., 2013, 2015). This tendency towards nanocrystallization poses significant challenges to the reliability of low-temperature viscosity measurements within the typical viscosity range of 10^8 to 10^{12} Pa s, complicating our understanding of magma dynamics.

Empirical viscosity models are generally designed to estimate the viscosity of nanolite-free melts. However, they often yield predictions that align more closely with the viscosity of nanolite-bearing melts (Di Genova et al., 2020a; Scarani et al., 2022a; Valdivia et al., 2023, 2024; Verdurme et al., 2023). This discrepancy complicates volcanic modeling, where high-quality viscosity data are essential for generating accurate probabilistic eruption scenarios (La Spina et al., 2021, 2016). In particular, viscosity measurements of supercooled volcanic melts at ambient pressure are crucial for quantifying the impact of structurally bonded volatiles, especially H_2O and CO_2, which significantly affect magma transport both chemically and physically (Di Genova et al., 2014a; Dingwell et al., 1996; Marxer et al., 2015; Mysen and Virgo, 1986; Richet et al., 1996, 2000; Stevenson et al., 1997; Whittington et al., 2001a; Zhang et al., 2003).

Additionally, the propensity for nanostructuration indicates that the structure of volcanic melts is more dynamic and chemically reactive than previously thought. Studies show that melts susceptible to nanoscale modifications can exhibit heterogeneous textures at the same scale, enhanced volatile degassing, and complex rheological behaviors (Cáceres et al., 2020; Di Genova et al., 2017a, 2020b, 2018; Mujin et al., 2017; Mujin and Nakamura, 2014, 2020; Okumura et al., 2022a, 2023, 2022b; Scarani et al., 2022a; Valdivia et al., 2024, 2023; Yoshida et al., 2022). This evolving structural scenario is crucial, especially since the SiO_2 content alone is no longer a definitive proxy of eruptive style (Giordano et al., 2009). Recent research highlights the central roles of FeO_T, TiO_2 and the Na_2O/K_2O ratio in controlling the relationship between melt structure and viscosity (Di Genova et al., 2017a, 2020b; Le Losq et al., 2017; Scarani et al., 2022a; Valdivia et al., 2023), leading to a more nuanced understanding of effusive versus explosive potential.

The Pozzolane Nere Plinian eruption (PNR, 407 ± 4 ka) in the Colli Albani volcanic district provides a unique case to explore these complexities. The PNR eruption released over 30 km^3 of tephri–phonolitic magma with high FeO_T (7.46 wt%) and TiO_2 (0.66 wt%), and elevated alkali levels ($K_2O = 9.09$ wt%; $Na_2O = 2.42$ wt%) (Campagnola et al., 2016). The unique chemistry of this magma, combined with its explosive nature, makes it an invaluable case study for understanding the interplay between melt structure, magma storage, transport and dynamics, and eruptive behavior in mafic systems.

In this study, we use Conventional and Flash–Differential Scanning Calorimetry (C–DSC and F–DSC) to determine the viscosity of PNR melts. By building upon prior literature, we present a new approach for characterizing the viscosity of both anhydrous and hydrous melts. We adopt a multipronged analytical methodology, using SEM–BSE imaging, FTIR, Raman, Mössbauer, and Brillouin spectroscopies to complement experimental measurements using conventional viscometry, C–DSC, and F–DSC.

Our findings demonstrate that PNR melt exhibits a high susceptibility to rapid nanostructuration, leading to the formation of Fe—Ti nanolites and a substantial threefold increase in viscosity. This increase cannot be attributed solely to the depletion of iron in the remaining matrix. Instead, the precipitation of nanocrystals induces a heterogeneous distribution of elements in the residual melt, producing a relatively SiO_2-enriched matrix and Al-enriched shells around the nanolites (Valdivia et al., 2023, 2024).

This redistribution of elements triggers a pervasive solid-like behavior and significantly alters the melt structure (Di Genova et al., 2020a, 2017a, 2020b; Valdivia et al., 2024). These findings challenge the assumption, often based on empirical models and incomplete sample characterization, that nanolite formation has a negligible effect on magma rheology (Kleest et al., 2020; Pereira et al., 2024; Wadsworth et al., 2024).

Our study introduces a new viscosity model for the PNR melt with varying water content (0–5 wt%). At an eruptive temperature of 1050 °C, our model predicts a 4300–fold increase in viscosity with decreasing water content; far exceeding predictions from empirical models (Giordano et al., 2008a; Langhammer et al., 2022) and surpassing the viscosity increases reported for similar melts in the literature. This discrepancy arises from two key factors: the increase in melt fragility with water content and the limitations of empirical viscosity models, which often rely on experimental data lacking rigorous textural and spectroscopic controls.

In conclusion, our paired experimental and analytical protocol provides a new combined approach for accurately measuring the viscosity of volcanic melts, capturing both structural and compositional influences on magma rheology. Additionally, our study offers insights into the storage, transport, rheological behavior and eruptive potential of PNR magma and, more broadly, into the behavior of mafic magmas involved in Plinian eruptions.

1.1. *Deriving melt viscosity by DSC; a review of the shift factor approach*

For decades, micropenetration and parallel plate viscometry have been widely employed to measure the viscosity of analogue and volcanic melts around the glass transition temperature (T_g) (Dingwell et al., 1996; Liebske et al., 2003; Richet et al., 1996; Romano et al., 2001; Sehlke et al., 2014; Stevenson et al., 2001; Vetere et al., 2007; Webb and Knoche, 1996; Whittington et al., 2001b). However, recent studies have highlighted that viscometry measurements near T_g can induce significant nanoscale structuring (including, but not limited to, nanocrystallization), loss of water from sample surface and iron oxidation in the melt (Di Genova et al., 2017a, 2020a; Kleest et al., 2020; Liebske et al., 2003; Okumura et al., 2022a; Scarani et al., 2022a; Valdivia et al., 2023, 2024). These alterations can drastically impact the derived melt fragility (Valdivia et al., 2023), thereby preventing accurate extrapolation of melt viscosity.

Differential Scanning Calorimetry (DSC) analysis provides a robust method for determining the viscosity of glass–forming melts that are susceptible to (nano)crystallization (e.g., Valdivia et al., 2023). This susceptibility can be readily identified by combining Raman spectroscopy with SEM imaging, as demonstrated in several studies (Al-Mukadam et al., 2020, 2021a; Cáceres et al., 2021; Cassetta et al., 2023a; Di Genova et al., 2018, 2023, 2020a, 2017a; Giuliani et al., 2024; Scarani et al., 2022a; Stabile et al., 2021; Valdivia et al., 2024, 2023; Zandonà et al., 2019a, 2019b, 2022a, 2023, 2022b).

Building upon the seminal work of Adam and Gibbs (1965) and the Narayanaswamy equations (Narayanaswamy, 1971), Scherer (1984) performed DSC measurements to elucidate the dependence of the fictive temperature T_f (Moynihan, 1995) on the cooling rate q $\left[log\left(\frac{1}{|q|}\right)\right]$ of an alkali lime silicate melt (NBS 710). Scherer (1984) demonstrated that this relationship parallels the equilibrium viscosity $[log(\eta)]$ through a constant known as the “shift factor”, quantified as $10^{11.3}$ Pa·K (Fig. 1). This parallelism aligns with the observed relationship between the cooling rate dependence of volume and the temperature dependence of viscoelastic properties (Bero and Plazek, 1991). The correlation can be

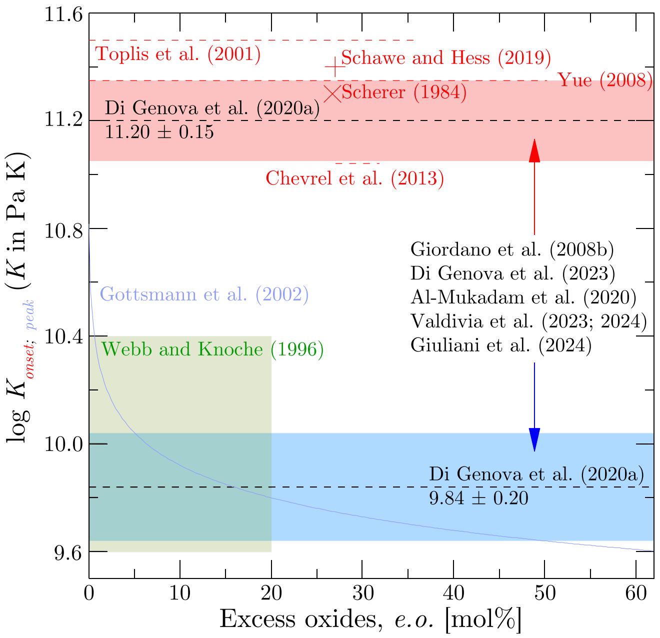

Fig. 1. Comparison of literature data for log K_{onset} and K_{peak} Eq. 2 obtained from silicate melts relevant to this study, plotted against the molar percentage of excess oxides (e.o.), as calculated following Gottsmann et al. (2002). The light red shaded area represents the uncertainty associated with the chemically independent K_{onset} (average value 11.20 ± 0.15 Pa·K, shown by the dotted black line) as identified by Di Genova et al. (2020a). Dashed red lines and symbols showing chemically independent K_{onset} values from the literature. The light blue shaded area indicates the chemically independent K_{peak} range (average value: 9.84 ± 0.20, shown by the dotted black line) from Di Genova et al. (2020a). The blue line shows the chemical dependence of K_{peak} according to Gottsmann et al. (2002). Red symbols and dashed lines indicate literature K_{onset} values. Studies confirming independent values K_{onset} = 11.20 Pa·K and K_{peak} = 9.84 Pa·K based on simultaneous DSC and viscometry measurements are listed in black. The plotted datasets include both viscometry and differential scanning calorimetry (DSC) data for silicate glasses. Additional data and analysis on systems relevant to technical glasses are discussed in the main text. (For interpretation of the references to colour in this figure legend, the reader is referred to the web version of this article.)

expressed as:

$$log_{10}\,\eta\left(T_f\right) = 11.3 - log_{10}(q) \tag{1}$$

where q is expressed in K·s^{-1}.

Scherer (1984) found that for moderate cooling rates, where $-1.5 \ll log_{10}(q) \ll 2.0$, Eq. (1) accurately predicts viscosity. However, at more extreme cooling rates, discrepancies emerge between the modelled viscosity based on Adam and Gibbs (1965) and the Arrhenian approximation of $log\left(\frac{1}{|q|}\right)$. This correlation has been validated as universal for more fragile basaltic melts over a broad range of cooling rate range, from 10^{-2} to 10^{6} K·s^{-1} (Yue et al., 2004) with the recalibrated shift factor $K_c = 10^{11.35}$ Pa·K (Fig. 1).

Subsequent studies (Yue, 2008) further confirmed the above–mentioned correlation by subjecting 17 silicate and 2 phosphate glasses with a wide range of fragilities (Angell (1995), with fragility index m from 83 to 167) to both viscometric and DSC experiments (Fig. 1). This work established a standardized unified approach for measuring the glass transition temperature (T_g) – defined as the temperature where viscosity $\eta = 10^{12}$ Pa·s – using DSC at a heating rate of 10 K·min^{-1} (onset temperature of the DSC upscan. See methodology for further details). Here, the fictive temperature T_f for hyperquenched glasses was determined using the enthalpy–matching method (Velikov et al., 2001; Yue et al., 2002). Notably, Eq. (1) implies that T_f is ≈ T_g when $q = 10$ K·min^{-1} ($log\ q = -0.78$ with q in K·s^{-1}).

The universality of Eq. (1) and the consistency of the shift factor $K_c \approx 10^{11.35}$ Pa·K have been extensively validated across various geological systems. Toplis et al. (2001) employed a constant $K_c = 10^{11.5}$ (Fig. 1) for several haplogranitic glasses using T_f. Independent shift factors have also been derived for a range of silicates, aluminosilicates, borosilicates and titanosilicates through dilatometric estimations of T_g (Sipp and Richet, 2002). Chevrel et al. (2013) derived T_f by DSC and found a $K_c = 10^{11.2\pm0.11}$ Pa·K for iron–free anorthite–diopside compositions, averaging $10^{11.04\pm0.37}$ Pa·K for iron–bearing systems (Fig. 1), aligning with prior literature within experimental error (Scherer, 1984; Sipp and Richet, 2002; Toplis et al., 2001; Yue, 2008). Zheng et al. (2017) collected T_g data from viscosity and DSC measurements of various compositions, including 20 boroaluminosilicate glasses, 6 soda–lime borate glasses, two fiber glass compositions, and 6 vanadium tellurite glasses. Their data confirms that the $K_c = 10^{11.20}$ Pa·K value is applicable across all tested compositions.

Al-Mukadam et al. (2020) introduced the term K_{onset} to describe the shift factor K_c, reporting a consistent $K_{onset} = 10^{11.19\pm0.06}$ Pa·K across various glass–forming silicate and fluorophosphate systems using both C–DSC and F–DSC (Fig. 1). Similarly, Schawe and Hess (2019) confirmed previous findings by determining $K_{onset} = 10^{11.40}$ Pa·K for standard soda–lime glass (Meerlender, 1974) using F–DSC (Fig. 1). Di Genova et al. (2020a) extended these findings to basalt from Mt. Etna (Italy) and five other compositions, including both fully polymerized and depolymerized silicate systems of interest for both geological settings and glass–ceramics applications, reporting a chemically–independent $K_{onset} = 10^{11.20\pm0.15}$ Pa·K (Fig. 1).

Inspired by Scherer (1984), subsequent studies (Gottsmann et al., 2002; Stevenson et al., 1995; Webb and Knoche, 1996; Wilding et al., 1995) adapted Eq. (1) by using a different characteristic temperature, termed "T_{gpeak}" —the peak of the heat flow over/undershoot— rather than T_f. Di Genova et al. (2020a) renamed this characteristic T_{peak} and introduced T_{end}, marking the end of the glass transition interval. Consequently, Eq. (1) was reformulated as:

$$log_{10}\,\eta\left(T_{onset,peak,end}\right) = K_{onset,peak,end} - log_{10}\left(q_{c,h}\right) \tag{2}$$

where $q_{c,h}$ represents the matching cooling/heating rate (K·s^{-1}) at which T_{onset}, T_{peak}, and T_{end} are measured via DSC. K_{onset}, K_{peak}, and K_{end} are the respective shift factors.

Webb and Knoche (1996) compiled T_{peak} data for 70 silicate melt compositions in the albite–anorthite–diopside, Na_2O–SiO_2, and haplogranitic (HPG8) systems (Fig. 1). In their study, T_{peak} was measured at 5 K·min^{-1} in DSC and volume expansion curves, with a corresponding melt viscosity at this temperature of $10^{11.22\pm0.33}$ Pa·s (i.e., average $K_{peak} = 10^{10.14}$ Pa·K) from 135 data. However, in their viscosity and DSC measurements of HPG8 melts solely carried out with the same laboratory equipment and identical thermal histories, they observed that K_{peak} ranged between $10^{9.6}$ and $10^{10.4}$ Pa·K. On the other hand, Stevenson et al. (1995) focused on SiO_2–rich melts like rhyolites and found that K_{peak} ranges from $10^{10.1}$ to $10^{10.8}$ Pa·K as a function of the agpaitic index $\left[\left(\frac{Na_2O+K_2O}{Al_2O_3}\right)\right]$, with an average K_{peak} of $10^{10.49}$ Pa·K (Fig. 1). Afterwards, (Gottsmann et al., 2002) focused on a wide range of melts with different compositions and described K_{peak} as a composition–dependent term equal to $10^{10.321-0.175ln(x)}$ Pa·K where x is the molar percentage of excess (network modifying) oxides (Fig. 1).

Recently, Di Genova et al. (2020a), using consistent laboratory conditions and identical thermal histories for all samples, demonstrated that the shift factors in Eq. (2) remain chemically invariant across a diverse chemical interval range from anorthite (50 mol% SiO_2) to lithium–aluminosilicate (75 mol% SiO_2), yielding $K_{onset} = 10^{11.20\pm0.15}$ Pa·K, $K_{peak} = 10^{9.84\pm0.20}$ Pa·K, and $K_{end} = 10^{9.21\pm0.24}$ Pa·K (Fig. 1). These values aligns with some previous studies (Scherer, 1984; Webb and Knoche, 1996; Yue, 2008), and have been corroborated (Fig. 1) by subsequent studies on multicomponent and technical melts (Di Genova et al., 2023; Giuliani et al., 2024; Scarani et al., 2022a; Stabile et al., 2021; Valdivia et al., 2023, 2024; Zandonà et al., 2023), with the partial exception of tellurite glass (Al-Mukadam et al., 2021a) which shows slightly lower $K_{onset} = 10^{10.77\pm0.06}$ Pa·K, whereas $K_{peak} = 10^{9.73\pm0.10}$ Pa·K is consistent with Di Genova et al. (2020a).

Al-Mukadam et al. (2021b) integrated C–DSC and viscosity data from literature with F–DSC measurements on Zr–based bulk metallic glasses (BMGs) Vitreloy 105 and AMZ4, confirming that the shift factors K_{onset}, K_{peak}, and K_{end} proposed by Di Genova et al. (2020a) apply to these metallic glass–forming alloys. Dingwell et al. (2022) observed instead a lower K_{peak} of $10^{7.95}$ Pa·K for carbonate melts, generally consistent with high compressibility as expected for carbonate melts.

Importantly, several recent studies have incorporated Raman spectroscopy measurements on glasses before and after DSC and viscometric analyses (Di Fiore et al., 2024; Di Genova et al., 2023; Giuliani et al., 2024; Scarani et al., 2022a; Stabile et al., 2021; Valdivia et al., 2023, 2024; Zandonà et al., 2023). This systematic approach has confirmed that viscosity derivation via both conventional and flash DSC can reliably span from T_g (10^{12} Pa·s) down to 10^{6} Pa·s with constant shifts factors. Recently, Cáceres et al. (2024) conducted viscometry and DSC measurements on a series of rhyolites and concluded that K_{peak} values reported by Gottsmann et al. (2002) are systematically underestimated by 0.26–0.32 log units but reaffirmed their chemical dependence. Since iron–bearing melts are prone to nanostructuration and changes in iron oxidation states during viscometry and DSC measurements, the absence of Raman spectra before and after these analyses precludes definitive conclusions regarding the chemical dependence of K_{peak}. Similar uncertainties apply to findings by (Wadsworth et al., 2024).

The shift factors $K_{onset} = 10^{11.20\pm0.15}$ Pa·K and $K_{peak} = 10^{9.84\pm0.20}$ Pa·K reported by Di Genova et al. (2020a) are also applicable to hydrous melts. Giordano et al. (2008b) compiled measurements of T_{onset} and T_{peak} as a function of $q_{c,h}$ (5, 10, 15, 20, 25 K min^{-1}) for hydrous iron–free melts in the anorthite–diopside system. Their findings suggest that, for a given $q_{c,h}$, viscosities at T_{onset} and T_{peak} are independent of chemical composition. Therefore, by applying Eq. (2) one can calculate chemically independent shift factors (K_{onset} and K_{peak}); $K_{onset} = 10^{11.20\pm0.03}$ Pa·K and $K_{peak} = 10^{9.78\pm0.02}$ Pa·K. These are consistent with results reported by Di Genova et al. (2020a) and earlier studies.

In conclusion, the extensive literature in glass–ceramics and volcanology consistently supports the chemical invariance of K_{onset}, K_{peak}, and K_{end} (Di Genova et al., 2020a) for several silicate systems. Nonetheless, for rhyolitic melts, a subtle chemical dependence of K_{peak} on the agpaitic index $\left[\left(\frac{Na_2O+K_2O}{Al_2O_3}\right)\right]$ has been observed (Gottsmann et al., 2002; Stevenson et al., 1995), indicating that composition–specific factors may influence the shift factor in high silica–rich, carbonate and tellurite systems. This underscores the need for further investigation into the role of melt composition in such cases.

Additionally, the tendency of volcanic melts to undergo nanocrystallization and iron oxidation (Valdivia et al., 2024 and references therein) presents a critical challenge, as these processes can influence viscosity and DSC measurements, the interpretation of results and the estimation of K_{onset}, K_{peak}, and K_{end}. Without careful consideration of these physicochemical factors, especially in studies lacking comprehensive analytical and spectroscopic support, conclusions about viscosity behavior and melt structure dynamics may be unreliable or non–unique. To address these challenges, future research should adopt a more rigorous, multifaceted approach, integrating at least Raman spectroscopy alongside traditional methods such as Conventional–DSC, Flash–DSC, viscometry, and SEM imaging. This comprehensive methodology will facilitate more accurate derivations of melt viscosity and better account for nanostructural changes occurring during analysis (e.g., Di Genova et al. (2020a); Scarani et al., 2022b; Valdivia et al., 2023; Zandonà et al., 2022b). Such a holistic approach will provide more experimentally sound conclusions and mitigate the risk of misinterpretation that arises when methodological shortcuts are taken.

2. Materials and methods

2.1. Synthesis of starting materials

The starting material used in this study is a homogeneous, crystal– and bubble–free glass from Campagnola et al. (2016), derived by melting natural ash–to–lapilli–sized pyroclasts from the Pozzolane Nere formation (PNR, 407 ± 4 ka). This formation represents one of the largest ignimbrites (Giordano and Team, 2010) in the history of the Colli Albani volcanic system (Rome, Italy).

To prepare hydrous glasses, the anhydrous PNR_0 glass was first crushed into powder and sieved into two grain–size fractions: <100 μm and 100–250 μm. These fractions were mixed in a 1:1 weight ratio to optimize grain packing and minimize porosity during the synthesis of water–bearing glasses at high temperature and pressure. Water–bearing glasses, containing between 0.41 ± 0.01 and 4.66 ± 0.05 wt% H_2O, were synthesized using a piston–cylinder (PC) apparatus at the Bayerisches Geo–Institut (BGI), University of Bayreuth, Germany. Distilled water was added to the dry glass powder, which was then sealed in $Au_{80}Pd_{20}$ capsules (4.6 mm inner diameter, 10 mm length) to minimize iron loss during synthesis. After welding and weighing, the capsules were heated overnight at 150 °C to check for water loss.

The glass synthesis was carried out at 1280 °C and 5–7 kbar under reduced oxygen fugacity conditions (<NNO + 0), with a dwell time of 24 h to ensure water homogenization within the samples. Quenching was performed at an average rate of ~130 °C s^{-1} by cutting off the heating power, while pressure was maintained via an automatic controller. Throughout this study, the samples are referred to by their measured water content in wt% (e.g., PNR_0 for the anhydrous sample, and PNR_4.66 for the sample with 4.66 ± 0.05 wt% H_2O).

The anhydrous reduced sample (PNR_0_RED) was synthesized by remelting PNR_0 powder in a gas-mixing furnace at 1400 °C under a CO_2:CO gas mixture ratio of 40:60, corresponding to an oxygen fugacity of approximately FMQ −2.5. The melt was held at these conditions for 8 h and subsequently quenched rapidly in water by melting a Pt wire, with the water container positioned at the bottom of the furnace.

2.2. Electron microprobe analyses

The chemical oxide composition (SiO_2, TiO_2, Al_2O_3, FeO_T, MnO, MgO, CaO, Na_2O, K_2O, and P_2O_5) of the samples was determined using a JEOL JXA–8200 electron microprobe at BGI (Table 1). The anhydrous and hydrous glasses were embedded in epoxy, polished, and carbon–coated before analysis. Measurements were conducted at an accelerating voltage of 15 kV, a current of 5 nA, using a 10 μm defocused beam, and a counting time of 20 s. To minimize alkali migration, Na and K were analyzed first with a shorter counting time of 10 s (Hughes et al., 2019).

Calibration standards included synthetic wollastonite (for CaO and SiO_2), periclase (MgO), hematite (FeO_T), spinel (Al_2O_3), orthoclase (K_2O), albite (Na_2O), manganese titanate (MnO and TiO_2), and apatite (P_2O_5). The resulting compositional data were consistent, within experimental uncertainty, with those reported in previous studies on the melt viscosity of the Pozzolane Nere from Colli Albani (Campagnola et al., 2016; Kleest et al., 2020).

2.3. Scanning electron microscope

High-resolution back-scattered electron (BSE) images of glasses were collected using a scanning electron microscope (SEM) at 20 kV accelerating voltage with a counting time of 20 s.

Table 1
Chemical composition (wt%) of the samples used in this study. Total FeO was measured by EMPA, with Mössbauer spectroscopy used to determine the FeO and Fe_2O_3 content. Water content was measured using FTIR spectroscopy. σ is the standard deviation.

Oxide	PNR_0	σ	PNR_0_RED	σ	PNR_0.41	σ	PNR_0.65	σ	PNR_0.86	σ	PNR_1.27	σ	PNR_1.85	σ	PNR_2.98	σ	PNR_4.66	σ
SiO_2	52.86	0.18	53.65	0.26	53.61	0.25	52.85	0.19	53.01	0.25	52.97	0.17	52.26	0.33	51.39	0.24	51.05	0.24
TiO_2	0.73	0.05	0.74	0.05	0.72	0.05	0.73	0.07	0.73	0.05	0.72	0.05	0.70	0.06	0.71	0.05	0.70	0.05
Al_2O_3	19.52	0.18	19.59	0.08	19.88	0.13	19.63	0.15	19.69	0.18	19.66	0.16	19.23	0.19	19.09	0.13	18.83	0.16
FeO	2.14	0.04	4.48	0.15	3.20	0.10	3.71	0.05	4.15	0.08	3.84	0.07	3.65	0.07	2.45	0.04	4.15	0.07
Fe_2O_3	4.62	0.09	1.17	0.04	1.18	0.04	2.31	0.03	1.45	0.03	1.55	0.04	1.71	0.04	4.09	0.07	1.88	0.03
MnO	0.18	0.04	0.18	0.03	0.18	0.03	0.19	0.03	0.18	0.04	0.19	0.03	0.18	0.03	0.19	0.04	0.18	0.03
MgO	2.23	0.05	2.27	0.06	3.17	0.14	2.31	0.08	2.29	0.06	2.29	0.08	3.05	0.16	2.16	0.08	2.31	0.06
CaO	5.59	0.09	5.65	0.10	5.72	0.10	5.53	0.10	5.55	0.08	5.50	0.09	5.44	0.11	5.42	0.09	5.37	0.09
Na_2O	2.28	0.09	2.32	0.07	2.27	0.13	2.26	0.08	2.34	0.12	2.28	0.12	2.22	0.10	2.25	0.10	2.21	0.10
K_2O	9.48	0.13	9.61	0.12	9.25	0.18	9.45	0.17	9.32	0.17	9.42	0.18	9.43	0.21	9.04	0.14	8.95	0.16
P_2O_5	0.37	0.06	0.34	0.10	0.38	0.08	0.38	0.06	0.36	0.08	0.37	0.08	0.39	0.04	0.35	0.06	0.34	0.08
H_2O	0.00	–	0.00	–	0.41	0.01	0.65	0.03	0.86	0.01	1.27	0.03	1.85	0.04	2.98	0.07	4.66	0.05
Fe^{3+}/Fe_T	0.66	0.02	0.17	0.01	0.23	0.02	0.39	0.03	0.25	0.01	0.33	0.01	0.36	0.02	0.49*	0.02	0.46*	0.02

PNR_0 and PNR_0_RED represent anhydrous samples quenched in air and under reduced conditions, respectively (see Methods).

* Iron oxidation state measured from a nanostructured sample.

2.4. Water content determination

The water content of the hydrous glasses was determined using Fourier–transform infrared spectroscopy (FTIR) at BGI, employing a Bruker IFS 120 spectrometer and a Bruker IR microscope. Spectra were collected with a tungsten white light source, a silicon–coated calcium fluoride beam–splitter, and a liquid–N_2–cooled narrowband mercury cadmium telluride (MCT) detector. Measurements covered the 1000 to 10,000 cm^{-1} range on doubly polished samples, with thicknesses between 0.06 and 0.3 mm. Each analyzed spot had a diameter of 60 μm, and spectra were recorded at a resolution of 4 cm^{-1}. A total of 200 scans per spectrum were accumulated, and measurements were taken at three different spots per glass sample to account for possible heterogeneity.

The total water content (H_2O_T) was derived from the areas of the hydroxyl (OH^-) and molecular water (H_2O_{mol}) bands, located around 4500 cm^{-1} and 5200 cm^{-1}, respectively. These peaks represent the stretching and bending modes of OH^- groups and water molecules (Bondar et al., 2023 and references therein). We applied a procedure as in Bondar et al. (2023) similar to the "two Gaussians" (GG) described by Ohlhorst et al. (2001) to subtract baselines from our spectra. Densities were calculated as follows: Using Eq. 1 and the recorded cooling rate of a half-inch piston-cylinder experiment (Bondar et al., 2020), a viscosity of $10^{9.19}$ Pa s at the fictive temperature (T_f) was obtained. The T_f was then determined using the viscosity model presented here. Densities at T_f were calculated with the *DensityX* software (Iacovino and Till, 2019), and room-temperature densities (Table 2) were estimated using the thermal expansion coefficient and its dependence on water content for phonolitic glasses (Bouhifd et al., 2001). Water contents were calculated employing peak areas and integral absorption coefficients calculated as a function of SiO_2 content of glasses (Ohlhorst et al., 2001).

2.5. Micropenetration viscometry (MP)

Plane–parallel anhydrous glass chips, each 3 mm thick, were used for micropenetration viscometry (MP) measurements. The penetration rate of a hemispherical iridium indenter was measured using a Setaram Setsys vertical dilatometer at the Experimental Volcanology and Petrology Laboratory (EVPLab) at the University of Roma Tre (Italy). An applied load of 120 g was used, with an instrument precision of ±0.06 log units. Standard procedures were followed to ensure thermal equilibration of the sample at the target temperature, as outlined by Di Genova et al. (2014a). The indentation depth was recorded over time, and the viscosity curve was derived using the following equation (Douglas et al., 1965):

$$\eta = \frac{3F}{16\sqrt{2rL}\ \frac{dl}{dt}} \tag{3}$$

where η is the Newtonian viscosity (Pa·s), F is the applied force (N), t is the time (s), r is the radius of the sphere (m), L is the cumulative indentation depth (m), and $\frac{dl}{dt}$ is the indentation within a measurement interval. To calibrate the dilatometer, viscosity measurements were performed on the standard glass DGG–1, ensuring that the results matched the certified viscosity data (Meerlender, 1974) within a deviation of ±0.1 log units.

2.6. Differential scanning calorimetry (DSC)

DSC analysis enables heat flow measurement and thus determination of the characteristic T_{onset} and T_{peak} of the glass transition interval (Fig. 2). T_{onset} is the intercept between the tangent to the specific heat capacity curve at constant pressure (C_p) in the glass region and the tangent at the inflection point during the glass transition (Fig. 2). T_{peak} represents the peak of the overshoot of the C_p curve in the glass transition region (Fig. 2).

Table 2

Glass transition temperature (T_g), water speciation (OH^- and H_2O_{mol}, wt%) and total concentration (H_2O_T, wt%), *K/G* ratio derived by Brillouin spectroscopy, and boson peak position (ω_{BP}) of PNR glasses.

Sample	n.	Density, (g/L)	T_g (°C)	C_{OH^-}[a] (wt%)	C_{H2Omol}[a] (wt%)	C_{H2OT} (wt%)	*K/G*[b]	m_{BLS}[c]	ω_{BP} (cm^{-1})[d]
PNR_0	–	–	646.8	–	–	–	1.58 ± 0.03	31.32 ± 1.31	54.46 ± 0.93
PNR_0_RED	–	–	626.7	–	–	–	1.58 ± 0.02	31.18 ± 0.86	54.82 ± 1.11
PNR_0.41	8	2698	575.8	0.41 ± 0.01	–	0.41 ± 0.01	1.56 ± 0.04	30.58 ± 1.72	54.22 ± 1.35
PNR_0.65	8	2704	558.1	0.56 ± 0.03	0.09 ± 0.02	0.65 ± 0.03	1.59 ± 0.03	31.84 ± 1.29	55.58 ± 1.32
PNR_0.86	7	2698	536.4	0.73 ± 0.00	0.13 ± 0.01	0.86 ± 0.01	1.60 ± 0.07	32.20 ± 3.01	57.56 ± 1.50
PNR_1.27	7	2682	508.0	0.95 ± 0.01	0.32 ± 0.02	1.27 ± 0.03	1.61 ± 0.02	32.46 ± 0.86	59.24 ± 1.60
PNR_1.85	6	2673	473.2	1.25 ± 0.01	0.61 ± 0.03	1.85 ± 0.04	1.63 ± 0.02	33.53 ± 0.86	59.78 ± 2.13
PNR_2.98	3	2627	426.4	1.79 ± 0.03	1.19 ± 0.09	2.98 ± 0.07	–	–	–
PNR_4.66	3	2610	376.4	2.12 ± 0.14	2.54 ± 0.10	4.66 ± 0.05	–	–	–

n: number of FTIR spectra collected for each sample

[a] FTIR results after Ohlhorst et al. (2001).

[b] From Eq. 7

[c] From Eq. 15

[d] From Eq. 5

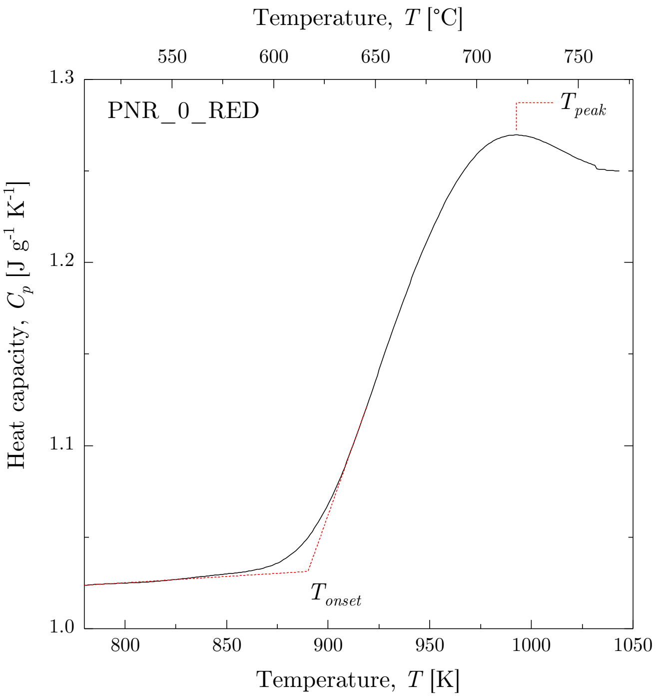

Fig. 2. Measured specific heat capacity at constant pressure (C_p) using a conventional DSC as a function of temperature for sample PNR_0_RED at a heating rate of 10 K min^{-1}, following a cooling rate of 10 K min^{-1} through the glass transition interval. The characteristic glass transition temperatures (T_{onset} and T_{peak}) are shown in the figure.

2.6.1. Conventional DSC (C–DSC)

Conventional differential scanning calorimetry (C–DSC) measurements were carried out at the EVPLab using approximately 15 ± 5 mg of glass in a platinum crucible under a constant nitrogen (N_2 5.0) flow rate of 30 ml min^{-1}. The measurements were conducted using a Netzsch 404 F3 Pegasus C–DSC, at heating rates of 10 to 20 K min^{-1}.

Calibration of the C–DSC was performed using the melting temperatures and enthalpies of fusion of standard reference metals (indium, tin, bismuth, zinc, aluminum, silver, and gold). To eliminate the thermal history of the samples, they were first heated at a rate of 20 K min^{-1} up to T_{peak} and then cooled to 100 °C at either 10 or 20 K min^{-1}. The C–DSC measurements were conducted using the rate–matching method, where an additional heating segment (upscan) was performed at the same rate as the preceding cooling segment (downscan).

2.6.2. Flash DSC (F–DSC)

The Flash DSC (F–DSC) measurements were conducted at the GLASS (Gateway Laboratory of Amorphous and Structured Solids and Melts), CNR–ISSMC in Rome. The F–DSC system is equipped with a UFH1 sensor, allowing for measurements up to 1000 °C and heating/cooling rates as high as 30,000 K s^{-1}. For this study, we used a heating rate of 1000 K s^{-1}, following methodologies outlined by previous studies (Al-Mukadam et al., 2020; Di Genova et al., 2023; Scarani et al., 2022b; Valdivia et al., 2023).

To optimize the signal–to–noise ratio, glass sample masses ranging from approximately 10 ng to 300 ng were used (Al-Mukadam et al., 2020). The F–DSC was calibrated using the melting points of aluminum (660.4 °C) and indium (156.6 °C) as standards. To impose a known thermal history to samples, glasses were heated at a rate of 1000 K s^{-1} up to their respective T_{peak}, followed by rapid cooling to 50 °C at the same rate (1000 K s^{-1}). As with the conventional DSC (C–DSC), F–DSC measurements were conducted using the rate–matching method to ensure consistency.

2.7. Raman spectroscopy

Raman spectroscopy was performed on glass samples both before and after DSC and micropenetration measurements to detect any potential alterations at the nano– and microscale, including changes in the iron oxidation state. Two confocal Raman microscopes were used: a Horiba LabRam HR 800 (532 nm diode green laser) at the EVPLab, and an Alpha300R WITec (457 nm blue solid–state laser) at GLASS.

The Horiba LabRam HR 800 yields a laser power on the sample surface of around 10 mW. Instrumental settings consisted of 1800 grooves mm^{-1} grating density, confocal hole of 300 μm and slit of 200 μm.

The Alpha300R WITec system featured a RayShield ultra–low frequency Raman filter, which was used for measuring the glass Boson peak (Cassetta et al., 2021). It is equipped with a crossed–polarized microscopy setup, enabling also the crossed–polarized spectra acquisition, and an ultra–high–throughput spectrometer with a 300 mm focal–length lens–based imaging spectrometer. The system has an optical fiber entrance and a motorized triple grating turret with two gratings (600 and 1800 lines/mm, blazed for 500 nm). The CCD camera is a high–efficiency, back–illuminated chip with a 1024 × 127–pixel format and 26 × 26 μm pixel size. The camera is Peltier–cooled to approximately −50 °C at a 20 °C ambient temperature, ensuring low noise and high performance. The power on the sample surface was set equal to 5 mW.

Raman spectra were acquired using a 100× objective, covering the silicate region (200–1500 cm^{-1} for the Horiba LabRam HR 800 and 0–1500 cm^{-1} for the Alpha300R WITec) and the water region (2700–4000 cm^{-1}). For the Horiba LabRam HR 800, an integration time of 30 s (with 6 accumulations). The parameters for the Alpha300R WITec system were 5 s acquisition and 3 accumulations. Both Raman spectrometers were calibrated using a silicon standard to ensure accurate and reliable measurements.

Alpha300R WITec Raman spectra were used to derive the boson peak position (Cassetta et al., 2021). Each spectrum was acquired with cross–polarized (HV) geometry (60 s and 10 accumulations) and corrected by applying a linear baseline to account for the weak luminescence background. To derive the Boson peak frequency position (ω_{BP}), the reduced Raman intensity $I^{red}(\omega)$ was calculated using the relation proposed by Shuker and Gammon (1970). This involves considering the Stokes side of cross–polarized (HV) Raman spectra and using the reduced Raman intensity expression:

$$I^{red}\ (\omega) = \frac{I_{mes}(\omega, T)}{\omega[n(\omega, T) + 1]} = C(\omega)\frac{g(w)}{\omega^2} \tag{4}$$

In this equation, $I_{mes}(\omega)$ is the Raman intensity, $n(\omega, T)$ is the Bose–Einstein population factor which accounts for the thermal population of vibrational modes at temperature (T) and frequency (ω), and $g(\omega)$ is the vibrational density of states, and $C(\omega)$ is the coupling function.

The reduced Raman intensity, $I_R(\omega)$, was then fitted with an asymmetric log–normal function Ando et al. (2018) to obtain the Boson peak frequency position (ω_{BP}). The fitting function used was:

$$I^{red}\ (\omega) = H \bullet exp\left(- ln(2)\left[\frac{ln\left(1 + 2a\frac{\omega - \omega_{BP}}{w}\right)}{a}\right]^2\right) + I_0 \tag{5}$$

where H is the amplitude, a is the asymmetry parameter, w is the width of the log–normal function and I_0 is an off–set parameter.

The goodness–of–fit was evaluated using the coefficient of determination (R^2) and the reduced chi–square value. Additionally, the residuals between the fitted function and the experimental data were inspected to ensure that the model appropriately captured the shape and asymmetry of the Boson peak.

2.8. *Mössbauer spectroscopy*

The iron oxidation state of all investigated samples was determined using Mössbauer spectroscopy. Glass chips of approximately 4 mm in diameter and 600 μm thickness were analyzed at BGI. Measurements were carried out at room temperature using a constant–acceleration Mössbauer spectrometer equipped with a high–activity ^{57}Co point source (370 MBq) embedded in a 12 μm thick Rh matrix. The velocity scale was calibrated relative to a 25 μm thick α–Fe foil, and data were acquired over a velocity range of ±5 mm s^{-1}. All Mössbauer spectra were fitted using a full transmission integral with pseudo–Voigt line shape and linear baseline implemented in the MossA software package (Prescher et al., 2012). Finally, the $\frac{Fe^{3+}}{Fe_T}$ ratio was calculated using the relative area associated with each iron species.

2.9. *Brillouin spectroscopy*

Brillouin spectroscopy (BLS) measurements were conducted at BGI on a plane–parallel polished glass sample, approximately 40–45 μm thick. A solid–state Nd laser (532 nm, 50 mW) was used to perform the measurements. The Brillouin frequency shift ($\Delta\omega$) was recorded with a six–pass Fabry–Pérot interferometer (Whitfield et al., 1976) and a single–pixel photon counter detector. A symmetric forward scattering geometry was employed with a scattering angle of $\theta = 79.8^\circ$ (Cassetta et al., 2021; Whitfield et al., 1976), and the scattering angle was calibrated using a silica reference glass.

Frequency shifts ($\Delta\omega$) were converted to longitudinal (v_p) and shear (v_s) sound velocities using the equation:

$$v = \frac{\Delta\omega\lambda}{2\,sin(\theta/2)} \tag{6}$$

where λ is the laser wavelength and θ is the scattering. For each sample, 4 to 8 spectra were collected at different rotation angles (from -180° to $+180^\circ$) to reduce uncertainties. The bulk–to–shear modulus ratio $\left(\frac{K}{G}\right)$ was calculated using:

$$\frac{K}{G} = \left(\frac{v_p}{v_s}\right)^2 - \frac{4}{3} \tag{7}$$

2.10. *Viscosity modeling*

The melt viscosity was parameterized as a function of temperature, $\eta(T)$, and water content using the Mauro–Yue–Ellison–Gupta–Allan (MYEGA) equation (Eq. 8) (Mauro et al., 2009):

$$log_{10}\eta(T) = log_{10}\eta_\infty + (12 - log_{10}\eta_\infty)\frac{T_g}{T}exp\left[\left(\frac{m}{12 - log_{10}\eta_\infty} - 1\right)\left(\frac{T_g}{T} - 1\right)\right] \tag{8}$$

where $log_{10}\eta_\infty = -2.93 \pm 0.3$ is the logarithmic viscosity at infinite temperature (Langhammer et al., 2021; Mauro et al., 2009), T_g is the glass transition temperature determined by C–DSC using T_{onset} at $q_h = 10\ K\ min^{-1}$ (see next paragraph), and m is the melt fragility. Melt fragility is defined by the slope of the viscosity curve at T_g in the Angell plot (Angell, 1995):

$$m = \left(\frac{\partial log_{10}\eta}{\frac{\partial T_g}{T}}\right)_{T=T_g} \tag{9}$$

To describe the dependence of T_g on water content, we used the model by Schneider et al. (1997), as adopted by Langhammer et al. (2021):

$$T_g(x_{H_2O}) = w_1 T_{g,H_2O} + w_2 T_{g,d} + c w_1 w_2 \left(T_{g,d} - T_{g,H_2O}\right) + d w_1 w_2^2 \left(T_{g,d} - T_{g,H_2O}\right) \tag{10}$$

where

$$w_1 = \frac{x_{H_2O}}{b(100 - x_{H_2O}) + x_{H_2O}} \text{ and } w_2 = \frac{b(100 - x_{H_2O})}{b(100 - x_{H_2O}) + x_{H_2O}} \tag{11}$$

Here, x_{H_2O} is the mol% of dissolved water, $T_{g,d}$ is the glass transition temperature of the anhydrous melt, and T_{g,H_2O} is the glass transition of pure water, equal to 136 K (Kohl et al., 2005). The parameters b, c, and d are fitting constants. This model incorporates the effect of water on $\eta(T)$ through T_g.

The melt fragility, m, for each water content was initially derived from BLS measurements following Cassetta et al. (2021) using (Eq. 12) and subsequently validated in the discussion section:

$$m = 43 \bullet \frac{K}{G} - 31 \tag{12}$$

3. Results and discussion

3.1. *Starting materials characterization*

Conducting a detailed nano– and microscale textural and chemical characterization of both the anhydrous and hydrous starting materials is crucial for accurately modeling the temperature– and water–dependent behavior of melt viscosity (Valdivia et al., 2023, 2024).

In this study, a combination of SEM–BSE imaging, Raman, FTIR, and Mössbauer spectroscopies was employed to quantify the water content and $\frac{Fe^{3+}}{Fe_T}$ ratio of the starting materials, as well as to establish either the amorphous or nanostructured nature (i.e., nanoscale phase separation or nanolite crystallization) of materials. Such an approach is particularly important given the chemical context of this study, where previous research has documented the presence of nanocrystals in glasses used for viscometry (Kleest and Webb, 2022), as well as in volcanic products from Colli Albani eruptions (Di Genova et al., 2020b).

In total, nine glass compositions were synthesized, with water contents up to 4.66 ± 0.05 wt% and $\frac{Fe^{3+}}{Fe_T}$ ratio varying from 0.17 ± 0.01 to 0.66 ± 0.02 (Tables 1 and 2).

The optical examination revealed no macrocrystals; however, in the sample with the highest water content (PNR_4.66), bubbles measuring 5–10 μm were observed, distributed inhomogeneously throughout the glass. Here, FTIR analyses were focused on bubble–free areas. SEM–BSE analysis revealed that all anhydrous and hydrous samples were free of micrometric crystals. However, in Raman spectroscopy, samples with the highest water contents, namely PNR_2.98 and PNR_4.66, displayed a characteristic spectral feature around 670 cm^{-1}, indicative of titanomagnetite nanolites (Di Genova et al., 2017a).

FTIR investigation of water speciation in these glasses indicates that the water dissolution mechanism generally aligns with that observed in basaltic glasses by Ohlhorst et al. (2001), with water primarily dissolved as hydroxyl groups at total H_2O contents below ~4 wt% and as molecular water above this threshold (Fig. 3). Notably, the speciation data shows a better fit for nanolite–free glasses, while nanolite–bearing glasses (empty crossed symbols in Fig. 3), particularly with inhomogeneously distributed bubbles, exhibit greater scatter in data points, as seen in the larger error bars. This suggests that water content determinations are less reliable for nanolite–bearing glasses.

Mössbauer spectroscopy provided insights into the iron oxidation states of the samples. Recorded spectra of PNR glasses show overlapping peaks representing different iron species (Fig. S1). Both divalent and trivalent iron species were fitted using either one or two doublets according to the goodness of fit. In general, all data appeared to be statistically resolved using a fitting model employing pseudo-Voigt line shapes for all Mössbauer features (Table S1). Uncertainties were determined based on the statistics of the fitting process. Anhydrous samples show a dominant quadrupole doublet as a major absorption peak ranging between 0.89 ± 0.04 and 1.1 ± 0.1 mm s^{-1} assigned to Fe^{2+} with a less intense feature at lower center shift (between 0.27 ± 0.02 and 0.46 ± 0.09) attributed to Fe^{3+}. Mössbauer spectra of hydrous samples exhibit a general increase in intensity for Fe^{3+} absorption peaks as a function of water content, with slight deviations from a linear trend. Overall, the obtained range of hyperfine parameters for Fe^{2+} and Fe^{3+} is aligned with what was previously reported for glasses (e.g., Trubowitz et al., 2024). The complete list of hyperfine parameters and a summary image of all recorded spectra for PNR glasses are provided in Table S1.

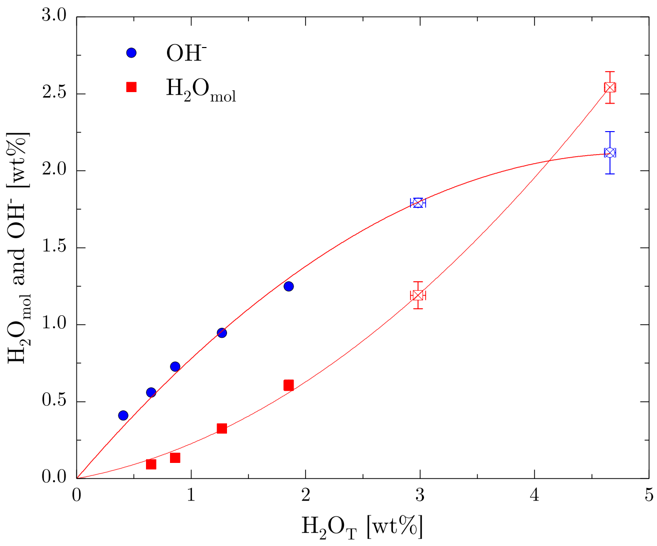

Fig. 3. Measured concentrations of molecular water (H_2O_{mol}) and hydroxyl groups (OH^-) plotted against total water content (H_2O_T) in PNR glasses. Error bars represent one standard deviation. The trendlines are forced to intercept at the origin. See text for further details. Empty symbols refer to nanolite-bearing samples.

$\frac{Fe^{3+}}{Fe_T}$ ratio of the samples was calculated considering the relative absorption areas of divalent and trivalent iron of the related Mössbauer spectra. The anhydrous glass quenched in air (PNR_0) was found to be the most oxidized $\left(\frac{Fe^{3+}}{Fe_T} = 0.66 \pm 0.02\right)$. In contrast, the anhydrous glass quenched under reduced conditions (PNR_0_RED) exhibited the highest degree of iron reduction $\left(\frac{Fe^{3+}}{Fe_T} = 0.17 \pm 0.01\right)$. For the hydrous glasses, a positive correlation between $\frac{Fe^{3+}}{Fe_T}$ ratio and water content was observed (Table 1). It is important to note that for nanolite–bearing samples (H_2O content >1.85 wt%), Mössbauer data are the result of a bulk measurement and therefore do not solely reflect the melt phase oxidation state since Fe–bearing nanocrystals are present (Bondar et al., 2025; Valdivia et al., 2023, 2024). Consequently, caution must be exercised when interpreting the $\frac{Fe^{3+}}{Fe_T}$ ratios of these samples.

The fitting of reduced HV Raman spectra of nanolite–free samples using Eq. 5 enabled the determination of the Boson peak position (ω_{BP}). Our results indicate that ω_{BP} shifts to higher wavenumber with increasing water content, ranging from 54.22 ± 1.35 cm^{-1} for PNR_0.41 to 59.78 ± 2.13 cm^{-1} for PNR_1.85 (Fig. 4A). As expected, the Boson peak was not observed in spectra of nanolite–bearing glasses, due to low amorphous–crystalline ratio.

3.2. Viscosity and fragility of PNR anhydrous melt

Micropenetration viscometry (MP) and Conventional Differential Scanning Calorimetry (C–DSC) measurements reveal that both the initial iron oxidation state and the measurement technique significantly influence the temperature dependence of melt viscosity, with important implications for viscosity modeling (Valdivia et al., 2023, 2024).

MP measurements were conducted on the anhydrous oxidized melt (PNR_0, $\frac{Fe^{3+}}{Fe_T} = 0.66 \pm 0.02$) at 691 °C and 780 °C. The starting PNR_0 glass is nanolite–free (Fig. 4B). Our measured viscosities (Fig. 5 A) compare well with previous data for the same composition (Campagnola et al., 2016; Kleest et al., 2020). However, Kleest et al. (2020) noted the presence of nanolites before MP viscometry using Raman spectroscopy, and observed that post–measurement spectra showed "an increase in nanolite content and a reduction in the typical glass 'hump' indicating nanolite growth." Similarly, we observed a time–dependent increase in viscosity at constant temperature during MP measurements, within the same temperature range studied by Campagnola et al. (2016) and Kleest et al. (2020). At 691 °C (Fig. 5A), the viscosity increased from $10^{11.85}$ to $10^{12.27}$ Pa·s over 60 min, while at 780 °C it rose from $10^{10.21}$ to $10^{10.58}$ Pa·s (Fig. 5A).

To further asses the reliability of the measured time–dependence of viscosity, we incorporated a reference glass standard (DGG–1). This glass, devoid of FeO and TiO_2, is known to exhibit stable, time–independent viscosity under similar experimental conditions. The viscosity of DGG–1 measured at 572 °C showed no time–dependent changes, confirming the absence of nanostructuration during MP measurements (Fig. 5B). This comparison underscores the robustness of our experimental approach, as the time–dependent increase in viscosity observed for PNR_0 is linked to melt nanostructuration, while the standard glass remained unaffected, validating the accuracy of our method in viscosity determination.

It is important to note that the initial viscosity values measured do

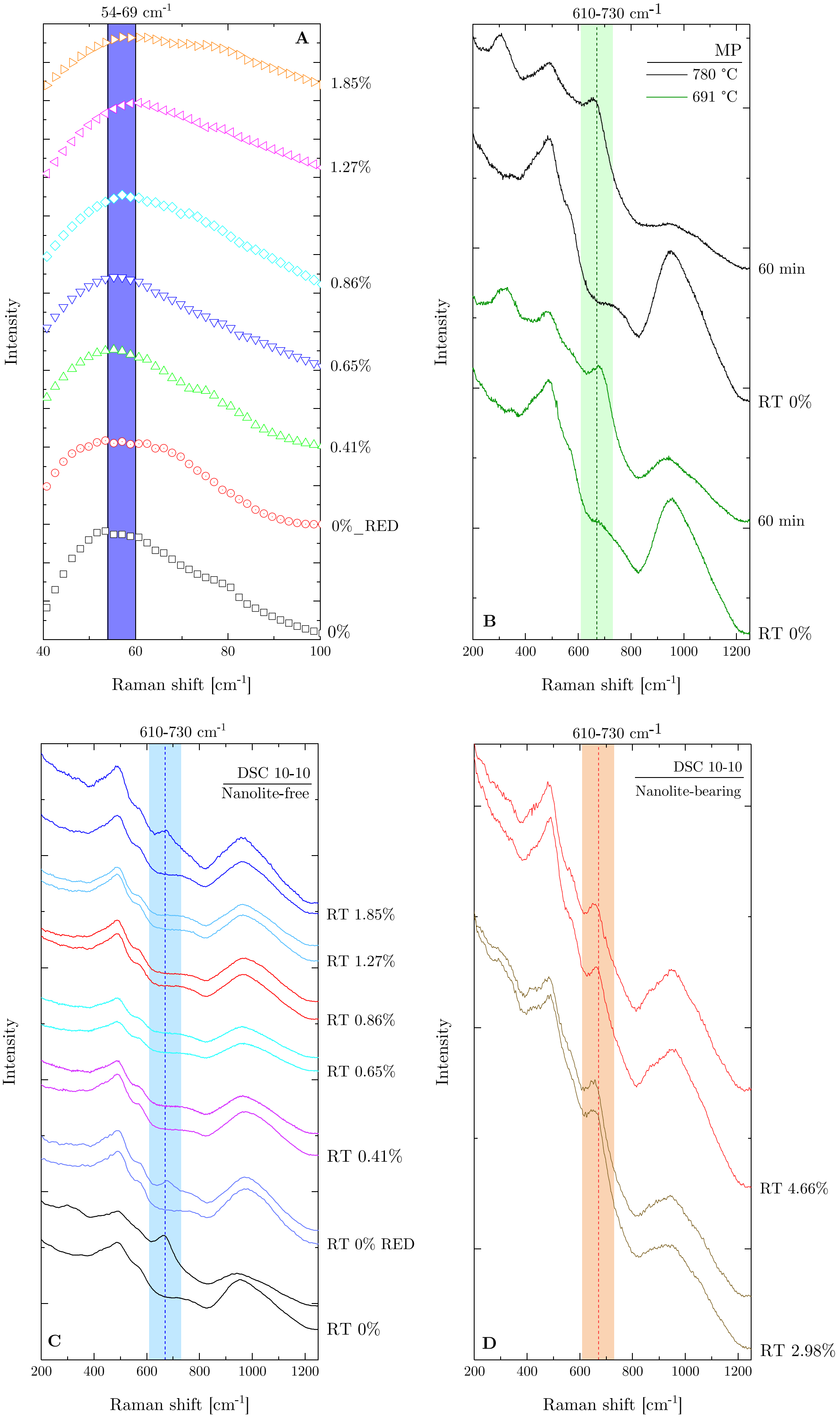

(caption on next page)

Fig. 4. Raman spectra of glass samples. A) Reduced Raman spectra of nanolite–free samples in the Boson peak region for the HV polarization geometry. The shaded region highlights the spectral variation of the Boson peak (Table 2), which shifts from lower to higher wavenumbers with increasing water content. B) Raman spectra of anhydrous samples before (RT 0 %) and after micropenetration (MP) viscometry (60 min). Notice the significant changes in the Raman spectra, indicating nanoscale structuring of the glass during MP. C) Raman spectra of the anhydrous (PNR_0 and PNR_0_RED) and hydrous starting materials (water content up to 1.85 wt%), which were free of nanolites before Differential Scanning Calorimetry (DSC) analysis. The top spectrum (collected at room temperature after DSC analysis) shows clear nanoscale structuring in the anhydrous oxidized (PNR_0) and hydrous (PNR_1.85) samples. D) Raman spectra of samples that were already nano-structured (i.e., nanolite-bearing) before the DSC measurements are shown. "RT" indicates room temperature, and the percentages represent the water content in weight percent (wt%). The shaded region (610–730 cm^{-1}) in B, C and D highlights the spectral range affected by nanoscale structuring of the glass (Di Genova et al., 2017a).

not correspond to nanolite–free viscosity, as post–MP Raman analyses revealed a pronounced peak at ~690 cm^{-1}, indicating nanocrystallization during MP experiments. The dwell temperatures for MP measurements are indeed significantly higher than the sample glass transition temperature ($T_g = 646.8$ °C, as determined below). Therefore, before reaching the target temperatures of 691 °C and 780 °C for MP measurements, the sample crosses T_g and undergoes nanostructuration during the heating phase, which takes several minutes. To mitigate this process, we employed the shift factor approach through C–DSC and F–DSC measurements, which subjects the sample to target temperatures for a shorter duration, therefore potentially limiting nanocrystallization (Valdivia et al., 2023).

We initially performed C–DSC measurements on the oxidized anhydrous PNR_0 sample $\left(\frac{Fe^{3+}}{Fe_T} = 0.66 \pm 0.02\right)$ at heating rates of 10 and 20 K min^{-1}, which confirmed the high propensity of the sample to nanocrystallize (Fig. 4C) as previously documented with micropenetration viscometry. At a rate of 10 K min^{-1}, T_{onset} and T_{peak} were 646.8 °C and 691.7 °C, respectively, while at 20 K min^{-1} they were 643.4 °C and 691.2 °C. This trend was unexpected, as higher heating rates must result in increased characteristic temperatures and could be related to nanocrystal formation as evidenced by post–measurements Raman spectroscopy (Fig. 4C). However, if we were to disregard the Raman results and assume $T_g = 646.8$ °C (T_{onset} at 10 K min^{-1}, as per (Yue et al., 2002)), then a notable mismatch appears between MP– and C–DSC–derived viscosity data. Specifically, T_g derived by MP viscometry from previous literature (Campagnola et al., 2016; Kleest et al., 2020), and from the Giordano et al. (2008a) model for PNR_0 are significantly higher (~700 °C). Nonetheless, nanocrystallization during viscometry has been documented in this temperature interval both in this study (Fig. 4C) and by Kleest et al. (2020). As such, 700 °C must be a temperature above T_g for PNR_0 melt.

Next, C–DSC measurements were conducted on the reduced anhydrous sample (PNR_0_RED, $\frac{Fe^{3+}}{Fe_T} = 0.17 \pm 0.01$) at heating rates of 10 and 20 K min^{-1}. As expected, the T_g of this sample was approximately 20 °C lower than that of PNR_0. However, unlike PNR_0, the T_{onset} values followed the expected trend, with T_{onset} at 20 K min^{-1} (631.2 °C) being higher than that at 10 K min^{-1} (626.7 °C, T_g). Despite this, Raman spectroscopy indicated that nanostructuration (either amorphous phase separation or nanocrystallization) occurred in this sample (Fig. 4C).

To describe the viscosity–temperature relationship for the anhydrous PNR melt, we employed the Mauro–Yue–Ellison–Gupta–Allan (MYEGA) parametrization (Mauro et al., 2009) (Eq. 8), using $\eta_\infty = 10^{-2.93}$ Pa·s (Langhammer et al., 2021; Mauro et al., 2009). The dataset used for

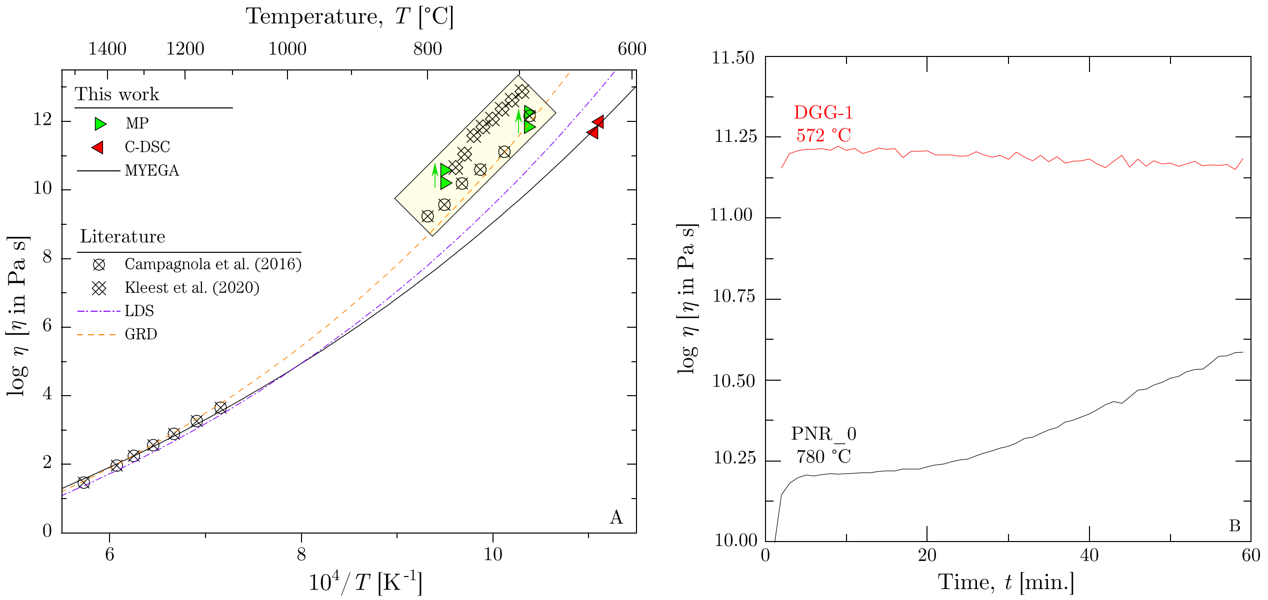

Fig. 5. Viscosity of PNR anhydrous samples. **A)** Viscosity of the anhydrous PNR sample as a function of temperature, compared with previous studies. Red, left–pointing triangles show low–temperature viscosity data derived from C–DSC measurements of the reduced sample (PNR_0_RED). Green, right–pointing triangles indicate viscosity measured via micropenetration (MP) over 60 min. The solid black line represents the MYEGA model fit (Eq. 8) for PNR_0_RED, using high–temperature viscometry data (concentric cylinder) from Campagnola et al. (2016). The fitting yielded a melt fragility index (m) of 31.32 ± 0.26 and T_g of 624.4 ± 2.0 °C. Crossed empty circles and diamonds represent low–temperature viscosity data from Campagnola et al. (2016) and Kleest et al. (2020), where nanolites were detected before MP measurements. The light–yellow rectangle highlights data influenced by nanolite formation before and/or during MP measurements. Dashed lines show viscosity predictions from the Giordano et al. (2008a) (GRD) and Langhammer et al. (2021) (LDS) models, with GRD predictions aligning with nanolite–bearing viscosity data. **B)** Time–dependent viscosity of the oxidized PNR_0 sample at 780 °C. The graph shows an increase in viscosity over time due to nanolite formation, which occurred at significantly lower temperatures than 780 °C as documented by C–DSC analysis (see text for details). The time–independent viscosity of the FeO– and TiO_2–free standard glass DGG–1 at 572 °C is included for comparison, highlighting the distinct difference in melt structure response during MP measurements, where no nanostructuration was observed. (For interpretation of the references to colour in this figure legend, the reader is referred to the web version of this article.)

fitting includes i) C–DSC–derived viscosity (Table 3) at T_{onset} for PNR_0_RED at 10 and 20 K min^{-1}, and ii) high–temperature viscometry data above the liquidus temperature from concentric cylinder viscometry by Campagnola et al. (2016). The fitting yielded a melt fragility index (m) of 31.32 ± 0.26 and T_g of 624.4 ± 2.0 °C, which are notably lower than the values obtained using literature low–temperature viscosity data (36.28 for m and 698.9 °C for T_g, Campagnola et al. (2016)) and the Giordano et al. (2008a) model (34.25 for m and 695.1 °C for T_g).

Overall, our MP–derived viscosity data (Fig. 5A), combined with literature date (Campagnola et al., 2016; Kleest et al., 2020), indicate that PNR_0 viscosity falls within the same temperature–viscosity range previously measured. These measurements, whether collected in this study or from literature, demonstrate that nanostructuration occurs during MP viscometry and even before (Kleest et al., 2020). As a result, viscosities obtained through MP measurements plot two log units higher than our MYEGA parameterization, which was formulated by combining high–temperature viscometry above the liquidus temperature with the most conservative estimate of T_g from the PNR_0_RED sample.

To conclude, we present an updated and well–constrained viscosity model for nanolite–free PNR anhydrous melt (Fig. 5A), developed to the best of our experimental capabilities. This model provides a more accurate and reliable framework for understanding the temperature–dependent viscosity of PNR melts, virtually free from the influence of nanoscale crystallization.

Table 3
Viscosity and DSC measurements of PNR melt.

Sample	Measurement[a]	T (°C)	log η (Pa s)
PNR_0	MP (0 min.)	691.0	11.85
	MP (60 min.)	691.0	12.27
	MP (0 min.)	780.0	10.21
	MP (60 min.)	780.0	10.58
	C-DSC$_{10\text{–}10\ \text{onset}}$	646.8	11.98
	C-DSC$_{10\text{–}10\ \text{peak}}$	691.7	10.62
	C-DSC$_{20\text{–}20\ \text{onset}}$	643.4	11.68
	C-DSC$_{20\text{–}20\ \text{peak}}$	691.2	10.32
PNR_0_RED	C-DSC$_{10\text{–}10\ \text{onset}}$	626.7	11.98
	C-DSC$_{20\text{–}20\ \text{onset}}$	631.2	11.68
PNR_0.41	C-DSC$_{10\text{–}10\ \text{onset}}$	575.8	11.98
	C-DSC$_{10\text{–}10\ \text{peak}}$	618.0	10.62
	C-DSC$_{20\text{–}20\ \text{onset}}$	581.3	11.68
	C-DSC$_{20\text{–}20\ \text{peak}}$	626.8	10.32
PNR_0.65	C-DSC$_{10\text{–}10\ \text{onset}}$	558.1	11.98
	C-DSC$_{10\text{–}10\ \text{peak}}$	597.3	10.62
	C-DSC$_{20\text{–}20\ \text{onset}}$	560.8	11.68
	C-DSC$_{20\text{–}20\ \text{peak}}$	604.4	10.32
PNR_0.86	C-DSC$_{10\text{–}10\ \text{onset}}$	536.4	11.98
	C-DSC$_{10\text{–}10\ \text{peak}}$	583.1	10.62
	C-DSC$_{20\text{–}20\ \text{onset}}$	541.6	11.68
	C-DSC$_{20\text{–}20\ \text{peak}}$	588.9	10.32
PNR_1.17	C-DSC$_{10\text{–}10\ \text{onset}}$	508.0	11.98
	C-DSC$_{10\text{–}10\ \text{peak}}$	554.1	10.62
	C-DSC$_{20\text{–}20\ \text{onset}}$	522.8	11.68
	C-DSC$_{20\text{–}20\ \text{peak}}$	569.0	10.32
PNR_1.85	C-DSC$_{10\text{–}10\ \text{onset}}$	473.2	11.98
	C-DSC$_{10\text{–}10\ \text{peak}}$	533.6	10.62
	C-DSC$_{20\text{–}20\ \text{onset}}$	480.9	11.68
	C-DSC$_{20\text{–}20\ \text{peak}}$	538.6	10.32
PNR_2.98	C-DSC$_{10\text{–}10\ \text{onset}}$	426.4	11.98
	C-DSC$_{10\text{–}10\ \text{peak}}$	474.4	10.62
	C-DSC$_{20\text{–}20\ \text{onset}}$	430.8	11.68
	C-DSC$_{20\text{–}20\ \text{peak}}$	499.5	10.32
PNR_4.66	C-DSC$_{10\text{–}10\ \text{onset}}$	376.7	11.98
	C-DSC$_{10\text{–}10\ \text{peak}}$	445.0	10.62
	C-DSC$_{20\text{–}20\ \text{onset}}$	384.9	11.68
	C-DSC$_{20\text{–}20\ \text{peak}}$	456.3	10.32

[a] MP = Micropenetration measurements taken at 0 and 60 min; C-DSC = Conventional Differential Scanning Calorimetry (DSC) performed at 10 and 20 K min^{-1}. The C-DSC values listed include the heating rates used (in K min^{-1}). The viscosities derived from C-DSC were calculated using the shift factor approach from Di Genova et al. (2020b).

3.3. Viscosity and fragility of hydrous melts

Due to the tendency of the anhydrous melt to undergo nanocrystallization, which would be enhanced by the presence of water (Valdivia et al., 2023), only C–DSC and C–FDSC measurements were carried out for the viscosity of hydrous glasses. Raman spectra collected post C–DSC measurements (Fig. 4C) confirmed the absence of significant nanostructuration in initially nanolite–free and less oxidized samples (H_2O and $\frac{Fe^{3+}}{Fe_T}$ ratio ranging between 0.41 and 1.27 wt%, 0.23 and 0.33, respectively). However, as we document in the next section, the thorough examination of the "Fe^{3+} band" and related regions of Raman spectra (Cassetta, 2024; Cassetta et al., 2025; Di Genova et al., 2016, 2017b; Le Losq et al., 2019) suggests that even minimal nanostructuration can still produce significant variations in viscosity. In contrast, Raman spectra of the sample with the highest water content (H_2O = 1.85 wt%, $\frac{Fe^{3+}}{Fe_T}$ = 0.36 ± 0.02) despite initially being nanolite–free, reveal clear evidences of nanocrystallization (Fig. 4C). Pre–existing nanolite–bearing samples (PNR_2.98 and PNR_4.66) showed no substantial changes in their Raman features after C–DSC measurements, irrespective of water content.

As expected, the glass transition temperature (T_{onset} at 10 K min^{-1}) decreased with increasing water content (Fig. 6, Table 2). For the anhydrous reduced sample (PNR_0_RED, $\frac{Fe^{3+}}{Fe_T}$ = 0.17 ± 0.01), T_g is 626.7 °C, while for PNR_4.66 (H_2O = 4.66 wt%, $\frac{Fe^{3+}}{Fe_T}$ = 0.46 ± 0.02), which initially contained nanolites, it dropped to 376.4 °C. This represents a T_g reduction of 250.3 °C upon the incorporation of 4.66 wt% of H_2O into the base anhydrous PNR composition.

Fig. 6 illustrates the decrease in T_g with water content and compares the measured data with predictions from two empirical models, GRD (Giordano et al., 2008a) and LDS (Langhammer et al., 2022). Both models overestimate the anhydrous T_g (624.6 °C), with LDS (667.6 °C) providing a closer estimate than GRD (695.0 °C). Both models perform reasonably well for predicting T_g in hydrous, nanolite–free samples. For water contents exceeding 3 wt%, where only nanolite–bearing samples

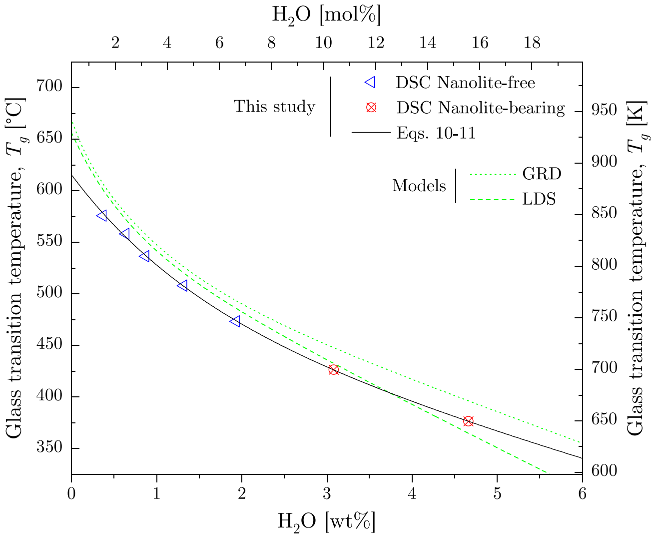

Fig. 6. Glass transition temperature (T_g, $\eta = 10^{12}$ Pa·s) as a function of water content (expressed in both wt% and mol%) measured via C–DSC. Blue left pointing triangles represent measured T_g from samples initially free of nanolite, while red crossed circles represent T_g data from samples initially containing nanolites. The black line represents the fit of the data using the model from Schneider et al. (1997), as applied by Langhammer et al. (2021) in Eqs. 10–11. The dotted and dashed lines correspond to the predictions from the GRD (Giordano et al., 2009) and LDS (Langhammer et al., 2022) empirical models, respectively. (For interpretation of the references to colour in this figure legend, the reader is referred to the web version of this article.)

were measured, the LDS model shows closer alignment with our data, while the GRD model predicts a higher T_g, consistent with values expected for nanolite–bearing samples.

Using Eq. 10 and 11, we parameterized T_g as a function of water content and obtained the fitting parameters $b = 0.255 \pm 0.043$, $c = 1.158 \pm 0.053$, and $d = -1.346 \pm 0.142$. This T_g model was then incorporated into the MYEGA parameterization (Eq. 8) to model PNR viscosity as a function of both temperature and water content. An Excel spreadsheet containing the model is provided as supplementary material.

Figure 7 shows the C–DSC–derived viscosity data for hydrous samples (Table 3) plotted against temperature in an Arrhenian format. It includes both nanolite–free and nanolite–bearing samples, with Arrhenian fits applied to describe the temperature dependence of viscosity. Broadly, the slope of the fit remains virtually consistent for the first four samples (0.41, 0.65, 0.86, and 1.27 wt% H_2O), which were initially nanolite–free and exhibited no significant nanostructuration (next section for more details) following C–DSC measurements (Fig. 4C). A noticeable change in slope is observed for the sample with 1.85 wt% H_2O, which experienced evident nanocrystallization during C–DSC as suggested by Raman spectroscopy (Fig. 4C). Further reductions in slope are observed in nanolite–bearing samples as water content increases.

These findings imply that melt fragility (m, Eq. 9) would decrease with increasing water content, suggesting that higher water content results in a ‘stronger’ melt (Angell, 1995), with less sensitivity to temperature–induced viscosity changes at elevated, volcanic temperatures. Both empirical models support this trend, with GRD predicting a significant decrease in melt fragility from 34.25 ($H_2O = 0$ wt%) to 26.14 ($H_2O = 4.66$ wt%), and LDS showing a similar decrease from 33.99 to 26.41 over the same water content range.

However, as demonstrated elsewhere (Valdivia et al., 2023), the anticipated decrease in fragility may not hold, possibly due to the complex interplay between water content and nanostructural rearrangements in the melt. Previous studies (Novikov and Sokolov, 2004; Scopigno et al., 2003) have shown that the vibrational properties of glass well below the glass transition temperature are correlated with melt fragility. This correlation allows the determination of melt fragility directly from the properties of the glass. Brillouin spectroscopy data (Table 2, Fig. 8), which provides the $\frac{K}{G}$ ratio (Eq. 7) — a recognized proxy for melt fragility (Cassetta et al., 2021, 2023b; Di Genova et al., 2023; Novikov and Sokolov, 2004; Valdivia et al., 2023) — shows a slight and linear increase with water content, yielding an average value of 1.60 ± 0.02. Despite relatively large error bars for individual measurements compared to the regression, the trend is consistent, indicating that the $\frac{K}{G}$ ratio, and therefore melt fragility, does not decrease with water content. The relationship has been parameterized as a function of water content (mol%) as:

$$\frac{K}{G} = 1.576\,(\pm 0.005) \bullet 0.029\,(\pm 0.004) \bullet H_2O \tag{13}$$

Notably, the Boson peak position (ω_{BP}) follows the same trend, namely ω_{BP} shifts to higher wavenumber with increasing water content (Fig. 8). This trend suggests that, unlike what observed in the viscosity curves, the fragility of the PNR melt may indeed increase with higher water content as also recently demonstrated for various synthetic and natural glass–forming melts (Cassetta et al., 2021). To conclude, and in line with these findings, the fragility extracted by viscosity data should not be considered correct as it is probably influenced by the presence and/or formation of nanolites. We propose that $\frac{K}{G}$ ratio and ω_{BP} measurements offer a best estimate of fragility, resulting here in a positive correlation of fragility index of PNR melts with water content.

In summary, our results indicate that the nanocrystallization tendency of PNR melt is primarily controlled by its initial water content, iron oxidation state, and the timescale of measurements above T_g. Nanocrystallization is more pronounced with increasing $\frac{Fe^{3+}}{Fe_T}$ ratio, increasing water content, and longer measurement durations, particularly for MP viscometry. Moreover, we suggest that the predicted reduction in fragility, as indicated by existing models, may be an artifact due to nanolite presence. This may have important implications for the accurate prediction of viscosity under eruptive conditions. Despite these complexities, the following section presents a model of PNR viscosity as a function of temperature and water content, using the MYEGA parameterization (Eq. 8). Our findings suggest that PNR melt may have a

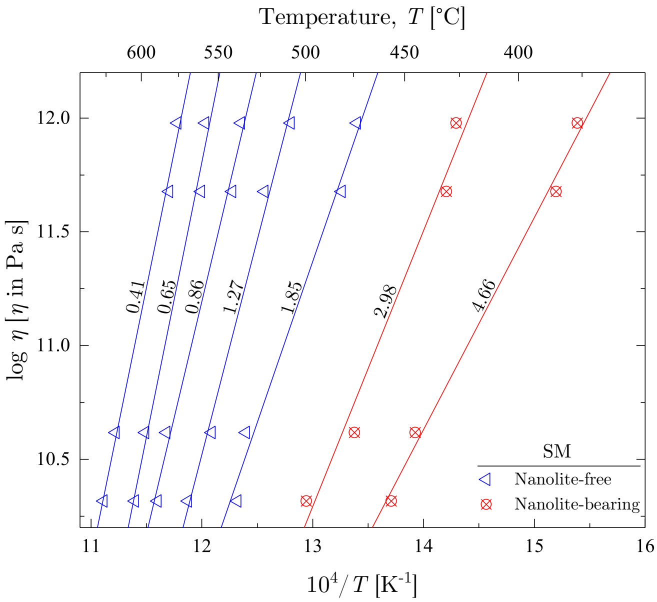

Fig. 7. C–DSC–derived viscosity of hydrous samples as a function of temperature. The numbers indicate the water content in each glass sample (wt%, see Table 1). Left–pointing triangles represent nanolite–free starting materials (SM), while crossed circles indicate nanolite–bearing SM. The lines represent Arrhenian fits to the data, highlighting the trend of decreasing melt fragility with increasing water content.

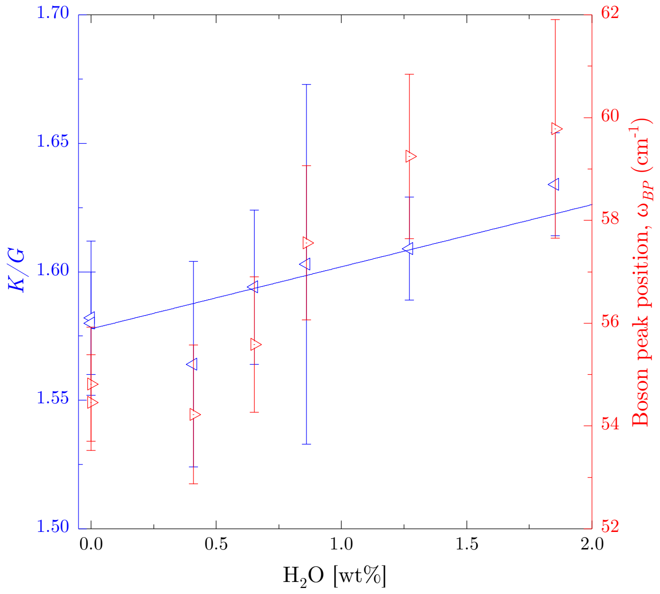

Fig. 8. $\frac{K}{G}$ ratio (left Y–axis) and boson peak position (ω_{BP}, right Y–axis) (Table 2) as a function of water content, measured via Brillouin spectroscopy and Raman spectroscopy, respectively. The blue line indicates the linear fit to $\frac{K}{G}$ data, described by the equation $\frac{K}{G} = 1.576\,(\pm 0.005) \bullet 0.029\,(\pm 0.004) \bullet H_2O$. For samples with water content higher than 1.85 wt%, $\frac{K}{G}$ ratio and boson peak position could not be measured due to the loss of glass transparency.

lower viscosity than previously anticipated (Campagnola et al., 2016; Giordano et al., 2008a; Kleest et al., 2020; Langhammer et al., 2022), which implies faster magma ascent rates and potentially more efficient coupling between phases in magmas (Valdivia et al., 2023). Additionally, the strong tendency of the PNR melt towards nanocrystallization is likely to influence magma dynamics in the upper conduit, contributing to the rapid viscosity increase during eruption (Di Genova et al., 2020b; Knafelc et al., 2022). Further discussion of volcanological implications in a broader context is provided below in a dedicated paragraph.

3.4. A viscosity model of anhydrous and hydrous PNR melt

Raman spectroscopy (Fig. 4B and C) demonstrates that the anhydrous, oxidized PNR_0 melt $\left(\frac{Fe^{3+}}{Fe_T} = 0.66 \pm 0.02\right)$ is highly prone to nanocrystallization during both micropenetration (MP) and differential scanning calorimetry (C–DSC) measurements. In the high–viscosity range ($10^8 < \eta < 10^{12}$ Pa·s, 5A), its viscosity aligns with literature data from studies that documented the presence of nanolites in the melt even before MP viscometry (Kleest et al., 2020). This viscosity is two to three orders of magnitude higher than what predicted by our anhydrous MYEGA parameterization (Fig. 5A). The MYEGA model was derived using nanolite–free viscosity data (Campagnola et al., 2016) and our C–DSC–based viscosity measurements of the reduced anhydrous melt $\left(\frac{\mathrm{Fe}^{3+}}{\Sigma\mathrm{Fe}} = 0.17 \pm 0.01\right)$. Our MYEGA model yields a glass transition temperature (T_g) of 624.6 °C and a melt fragility (m) of 31.33. A viscosity calculator is provided as Supplementary Material.

Our findings suggest two key points: (i) high–viscosity data from previous studies (Campagnola et al., 2016; Kleest et al., 2020) likely reflect an important contribution of nanolites to melt viscosity, and (ii) nanolite formation increases viscosity by up to 1000 times, consistent with observations in SiO_2–poor systems where this phenomenon was investigated exclusively in silicate melts (Di Genova et al., 2020a; Scarani et al., 2022a; Valdivia et al., 2023, 2024), which quantified the viscosity increase in the absence of microlites. Furthermore, the fragility of our anhydrous melt ($m = 31.32$) appears overestimated by the Cassetta et al. (2021) model based on Brillouin–derived $\frac{K}{G}$ ratio (Table 2). We propose a modified equation for the Cassetta et al. (2021) model, calibrated for PNR melt:

$$m = 43 \bullet \frac{K}{G} - 36.74 \tag{14}$$

This shift in the intercept matches the fragility values derived in our study.

Using the $\frac{K}{G}$ ratios from hydrous samples (Table 2), we derived the fragility index, m, for water content up to 1.85 wt% (Table 2), enabling an extended parameterization of PNR viscosity as a function of temperature (Fig. 9A). Additionally, based on the observed linear relationship in Fig. 8 between $\frac{K}{G}$ and water content in mol%, we parameterized m as a function of H_2O content (mol%) using a linear fit:

$$m = 31.10\ (\pm 0.27) + 0.27\ (\pm 0.05) {*} H_2O \tag{15}$$

where H_2O is in mol%. Below, we use this relationship between 0 and 5 wt% (0 and 16.6 mol%).

This approach enables us to model the viscosity of the PNR melt over a broad range of temperatures and water contents, and to compare our predictions with those from the GRD and LDS models (Fig. 9B).

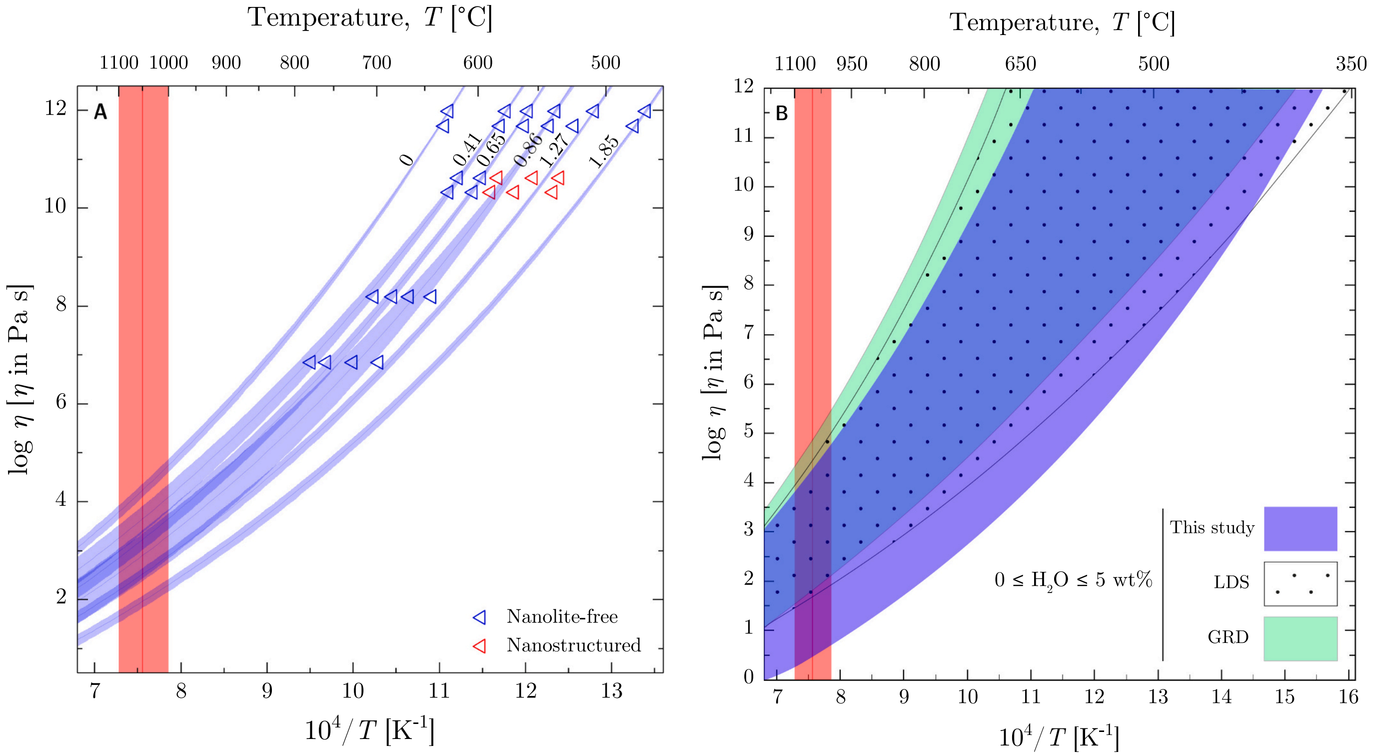

Fig. 9. A) Viscosity data for anhydrous and hydrous PNR samples. The blue lines represent the MYEGA parameterization (Eq. 7) using the glass transition temperature (T_g, Table 2) measured via C–DSC and melt fragility (m, Table 2) determined via Brillouin spectroscopy. The shaded areas indicate error propagation due to uncertainties in m (Table 2). Blue left–pointing triangles represent viscosity data from samples initially free of nanolites, red left–pointing triangles represent initially nanolite–free samples that underwent nanostructuration during C–DSC measurement (PNR_0.86, PNR_1.27 and PNR_1.85). As samples containing more than 1.85 wt % H_2O were not transparent to Brillouin spectroscopy, MYEGA models could not be derived for them. B) Global viscosity model for PNR melt as a function of water content (0 to 5 wt%) and temperature. The MYEGA model incorporates the T_g and m dependence on water content, as discussed in the text. In both figures, the red–shaded vertical area marks the expected eruptive temperature interval (1000–1100 °C) for PNR magma. (For interpretation of the references to colour in this figure legend, the reader is referred to the web version of this article.)

Specifically, Fig. 9B illustrates the temperature–viscosity space for the PNR melt containing between 0 and 5 wt% H_2O. We identified an interval between 1000 and 1100 °C as the expected eruptive temperature range for the mafic PNR magma. At an average temperature of 1050 °C (Jorgenson et al., 2024), our model predicts a substantial increase in viscosity from $10^{0.62}$ Pa·s to $10^{4.25}$ Pa·s as the water content decreases from 5 wt% to 0 wt%, representing a dramatic 4300–fold increase in viscosity. Such change can have a profound impact on magma transport dynamics, an issue we will explore in the following section. In comparison, the GRD model predicts substantially smaller viscosity increases over the same temperature and water content range for Italian alkaline magmas with similar $SiO_2 + Al_2O_3$ content, such as Pompei phonolite (1200-fold) and Minopoli shoshonite (341-fold) (Giordano et al., 2009). When extending the comparison to all available viscosity data from Italian volcanic melts at eruptive temperatures (Giordano et al., 2009), the PNR melt demonstrates the largest recorded change in viscosity with varying water content.

In contrast, the GRD and LDS empirical models predict notably lower increases in viscosity. The GRD model shows an increase from $10^{1.82}$ Pa·s to $10^{4.86}$ Pa·s (a 1090–fold increase), while the LDS model indicates an increase from $10^{1.65}$ Pa·s to $10^{4.44}$ Pa·s (a 610–fold increase). This strong contrast underscores the importance of capturing the water–dependent viscosity and especially the fragility of the PNR melt in refining our understanding of its rheological behavior and thereby of its eruptive dynamics.

Our Brillouin and Raman spectroscopy results (Fig. 8) indicate that fragility increases with water content (Table 2), a trend that contrasts with empirical predictions (Giordano et al., 2008a). However, previous studies on FeO– and TiO_2–bearing systems suggest that these empirical predictions may be influenced by nanocrystallization (Di Genova et al., 2020a; Kleest et al., 2020; Okumura et al., 2022a; Scarani et al., 2022a; Valdivia et al., 2023, 2024; Verdurme et al., 2023), which complicates their use for accurate viscosity and thus melt fragility estimates.

The relationship between water content and fragility is critical because fragility controls the temperature dependence of viscosity, a key factor in magma transport and timescales of physico–chemical processes such as element diffusion, nucleation, and melt relaxation. This water–dependence of fragility is further explored in the following section by examining both theoretical and experimental data.

Melt fragility (m) is a kinetic property that positively correlates with the degree of structural depolymerization, described for instance by $\frac{NBO}{T}$ (Mysen et al., 1985), and configurational heat capacity $C_p^{conf}(T_g)$ at the glass transition temperature. Previous studies (Bouhifd et al., 2006, 2013; Di Genova et al., 2014b; Giordano et al., 2015; Robert et al., 2014a) have shown a positive correlation between $\frac{NBO}{T}$ and $C_p^{conf}(T_g)$ in FeO– and TiO_2–free systems, where water addition increases $\frac{NBO}{T}$. Therefore, the addition of water would be expected to also increase m. However, contrary to this expectation and as reported earlier, the opposite is systematically observed when m is derived from viscosity fits using hydrous data of FeO– and TiO_2–bearing systems. Due to the tendency of hydrous melts to nanocrystallize, we were unable to directly measure $C_p^{conf}(T_g)$. However, (Robert et al., 2014b) documented that $C_p^{conf}(T_g)$ increases with water content in Fe- and Ti-free systems chemically similar to PNR melt. This consistency between increased fragility and heat capacity reinforces the reliability of our model. A similar conclusion was drawn by Cassetta et al. (2021) for trachyte systems.

Further validation of the water–dependence of fragility comes from our C– and F–DSC data. For nanolite–free samples (0.41, 0.65, 0.86, and 1.27 wt% H_2O), the MYEGA model (Fig. 9A) accurately predicts viscosities not used to calibrate the model, namely those from C–DSC data at both 10 K min^{-1} (T_{peak}) and 20 K min^{-1} (T_{onset} and T_{peak}) heating rates. This holds for the much lower viscosities obtained from F–DSC at 1000 K s^{-1} ($10^{8.19}$ Pa·s and $10^{6.84}$ Pa·s). Essentially, determining T_g from C–DSC and fragility from Brillouin spectroscopy allows for precise prediction of nanolite–free viscosity over a broad range of temperatures and water contents. This has been recently confirmed also for peridotitic melts (Di Genova et al., 2023).

A close inspection reveals that slight deviations from the MYEGA predictions are observed for sample PNR_1.27 % during C–DSC at high temperatures (569.0 °C, $10^{10.32}$ Pa·s namely T_{peak} 20 K min^{-1}), which we attribute to post–DSC iron oxidation and nanostructuration yielding higher viscosity, as indicated by changes in Raman spectra (Fig. 10). These changes are specifically identified by: i) sharpening and centering of the 800–1200 cm^{-1} region at around 970 cm^{-1} (Fe^{3+} band, (Di Genova et al., 2017b)) ii) a decrease in the 1040 cm^{-1} shoulder (reflecting a decreasing in $\frac{Fe^{3+}}{Fe_T}$, (Di Genova et al., 2017b)), and iii) a combined decrease in the 970 cm^{-1} intensity with an increase at 670 cm^{-1}, suggesting both nanostructuration and iron oxidation (Di Genova et al., 2016; Le Losq et al., 2019; Valdivia et al., 2024, 2023).

In conclusion, our MYEGA model accurately predicts the viscosities of PNR melts that are initially free of nanolites or remain unaffected by significant nanostructuration during viscosity measurements (Fig. 9A). Under eruptive conditions of temperature (Jorgenson et al., 2024) and water content, the PNR melt is one log unit less viscous than indicated by empirical models (Fig. 9B), which is likely to have substantial effects on magma storage and ascent dynamics, including ascent velocity and the coupling between the melt, crystals, and gas phases. Moreover, the observed relationship between melt fragility and water content aligns with theoretical predictions and insights into structural dynamics, thereby challenging the reliability of traditional micropenetration viscometry for establishing precise relationships between melt properties and structure.

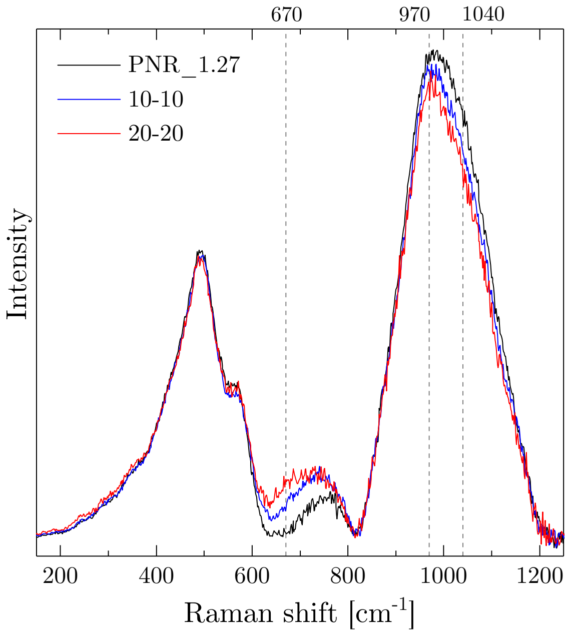

Fig. 10. Area normalized Raman spectra of PNR_1.27 before (black) and after C–DSC measurements at 10 (blue) and 20 K min^{-1} (red). The vertical dashed lines highlight regions where relative spectral intensity changes occurred in samples subjected to C–DSC analysis. These changes indicate iron oxidation (970 and 1040 cm^{-1}) and nanostructuration (670 cm^{-1}), which contribute to the viscosity increase observed in this sample. See text for further details. (For interpretation of the references to colour in this figure legend, the reader is referred to the web version of this article.)

3.5. From laboratory to volcano: Implications for magma transport at depth and Plinian mafic eruptions

The storage and eruptive conditions (temperature and dissolved water content) of the magma during the Pozzolane Nere (PNR) eruption remain uncertain. In Fig. 9B, we identified a temperature range expected for the PNR magma eruption (Campagnola et al., 2016), while Fig. 11 illustrates the variation in viscosity as a function of water content at an estimated average eruptive temperature of ~1050 °C. Our viscosity model reveals exceptionally low viscosity at 5 wt% dissolved H_2O, followed by a 4300–fold viscosity increase with near–isothermal H_2O loss. While the impact of water on magma viscosity is well established, the magnitude of the increase observed for the PNR melt significantly exceeds that of similar Italian systems (Giordano et al., 2009). These comparisons underscore the distinctive rheological behavior of the PNR melt, highlighting its highly fluid nature at depth and the pronounced effect of water exsolution on this mafic magma. This increase in viscosity is expected to intensify due to rapid crystallization in the conduit, with nanoscale crystallization tendencies documented here and microscale crystallization tendencies observed in prior studies (Campagnola et al., 2016). While the precise timing of nanolite formation in natural systems remains uncertain, it is likely a late-stage process occurring in the upper conduit under conditions of high undercooling, elevated nucleation rates, and limited growth. Our study focuses instead on the tendency of the PNR melt to rapidly crystallize and provides a model of the pure liquid viscosity, which has direct implications for the rapid crustal transfer of magma and pre-eruptive dynamics.

The Colli Albani volcanic complex is arguably the most explosively active mafic system, having produced at least seven VEI 6–7 caldera–forming eruptions despite the low silica contents of 42–53 % (Conticelli et al., 2010; Giordano et al., 2006; Palladino et al., 2001). This raises ongoing questions about the factors allowing such sustained explosivity. Some studies propose CO_2 sourced from carbonate basement interaction as a contributing factor (Freda et al., 2011); however, isotopic and petrologic analyses (Boari et al., 2009; Jorgenson et al., 2024) suggest that carbonate interaction likely influences only short–lived eruptions, not large caldera events at Colli Albani. Other research suggests that mantle–derived CO_2 sparging may promote leucite crystallization in shallow magma chambers, affecting rheology and promoting explosivity (Vinkler et al., 2012).

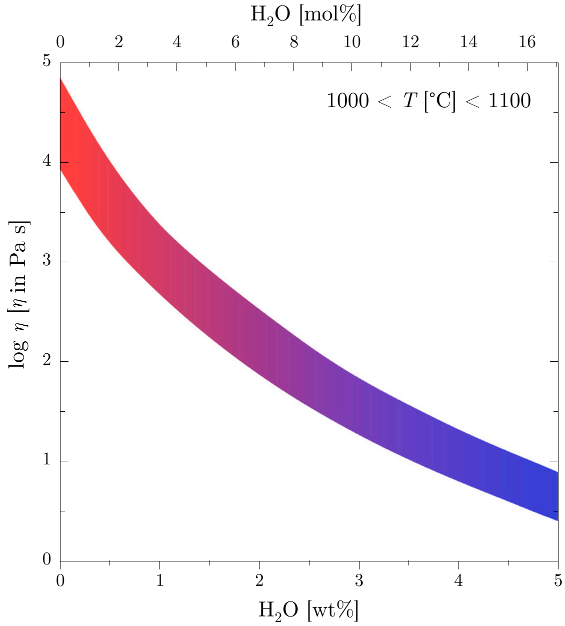

Fig. 11. Viscosity of PNR melt as a function of water content within the expected eruptive temperature range of 1000 to 1100 °C. The plot illustrates a significant variation (approximately 4300–fold) in viscosity with decreasing water content, highlighting the remarkable response of the melt to changes in water concentration under eruptive conditions.

Another challenge at Colli Albani involves understanding the long–term storage of hot mafic magma needed for caldera–forming eruptions, which recur approximately every 40,000 years (Karner et al., 2001). Cashman and Giordano (2014) proposed that magma could reside across multiple crustal levels within a transcrustal mush, interconnected shortly before or during eruptions. This would suggest that deeper reservoirs (>10 km depth) may be more stable, while shallow magma chambers (<10 km depth) are ephemeral, fed by deeper magma pulses (Cashman et al., 2017; Giordano and Caricchi, 2022). Jorgenson et al. (2024) identified high *Mg#* and high Cr_2O_3 clinopyroxenes in Colli Albani ignimbrites, which indicate rapid ascent from the mantle and suggest decadal to millennial storage times at 1200 °C before the eruption, underscoring the potential for rapid magma transfer and brief residence at shallow depths.

Our viscosity data for Pozzolane Nere provides a robust tool for assessing magma transfer rates under near–liquidus conditions (i.e., subliquidus). Specifically, we focus on the transfer of magma from deep mantle-crust boundary depths to shallower magma reservoirs, where magmas are typically liquid-dominated due to near-liquidus conditions or slight superheating (First et al., 2020; Marsh and Kantha, 1978). To estimate these rates, we applied a two-dimensional dyke flow equation (Arzilli et al., 2022; Lister and Kerr, 1991):

$$h = \left(\frac{3\eta Q}{2\Delta\rho g}\right)^{\frac{1}{3}} \tag{16}$$

where h is the dyke half–width, η the melt viscosity, $\Delta\rho$ the density contrast, g gravitational acceleration, and Q the magma discharge rate. We investigated a range of dike widths between 30 and 100 cm, which are representative of dike dimensions at depths greater than 10 km (Delaney and Pollard, 1982; Gonnermann and Taisne, 2015; Lister and Kerr, 1991). For the density contrast between magma and country rocks, we assumed a magma density of 2300 Kg m^{-3}, which is representative of hydrous tephri-phonolitic melts (Seifert et al., 2013), while the density of the country rocks was taken to be 2700 Kg m^{-3}, representative of granitic rocks. Based on the melt viscosity derived from the viscosity model presented in this study, our results indicate discharge rates ranging from 3 to 110 m^2 s^{-1}, which are notably higher than those predicted by the GRD model (0.1 to 3 m^2 s^{-1}). Additionally, given that it is unlikely for magma to be transferred solely along a single dike, these findings support the hypothesis of rapid magma ascent and the potential for high-volume, swift magma transfers.

While these findings do not model Pozzolane Nere conditions directly, they align with increasing petrologic evidence for fast magma migration and transient storage before caldera–forming eruptions (Allan et al., 2013; Carrasco-Núñez et al., 2018; Druitt et al., 2012; Gualda and Sutton, 2016; Gualda et al., 2012; Jorgenson et al., 2024; Pamukcu et al., 2015; Shamloo and Till, 2019; Wiebe et al., 2021; Wotzlaw et al., 2015). We emphasize the importance of well–constrained viscosity data for accurately modeling crystal–free or crystal–poor magma transport through transcrustal systems, particularly for deep–to–shallow magma transport before eruption. Such data are essential for estimating magma accumulation rates in deeper and shallower reservoirs, thereby advancing our understanding of caldera unrest and explosive potential (Giacomuzzi et al., 2024; Le Mével et al., 2015).

4. Conclusions

We successfully parameterized the viscosity of Pozzolane Nere (PNR) tephri–phonolitic magma from the Colli Albani volcanic system across a range of temperatures and water contents, demonstrating that PNR melt undergoes a substantial increase in viscosity with water exsolution. A viscosity calculator is provided as Supplementary Material. At an eruptive temperature of 1050 °C, our model predicts a dramatic 4300–fold increase in viscosity, a change that far exceeds predictions from empirical models and the behavior observed in other Italian volcanic melts. This discrepancy is attributed to two main factors: the increase in melt fragility with water content and the limitations of empirical viscosity models based on experimental data lacking rigorous textural and spectroscopic constraints. The observed correlation between melt fragility and water content is further substantiated by experimental data, spectroscopic analysis, and theoretical foundations of molecular structure of glass. Our experimental protocols provide a reliable method for measuring the viscosity of volcanic melts, accounting for both structural and compositional factors that influence magma rheology.

This study also offers new insights into the rheological behavior, transport at depth, and eruptive potential of PNR magma and, more broadly, of mafic magmas involved in Plinian eruptions. We show that the PNR melt is highly fluid at depth, which likely facilitates rapid magma storage and migration within the transcrustal magma plumbing system before caldera–forming eruptions. In turn, this fluidity supports fast magma ascent rates during eruptions. Additionally, we demonstrate that PNR melt exhibits a high susceptibility to rapid nanostructuration, resulting in the formation of Fe—Ti nanolites and a marked increase in melt viscosity. These combined factors upon magma ascent likely contribute to the explosive behavior of PNR magma.

CRediT authorship contribution statement

E. Fanesi: Writing – review & editing, Methodology, Investigation, Formal analysis, Data curation. **D. Di Genova:** Writing – review & editing, Writing – original draft, Visualization, Validation, Supervision, Resources, Project administration, Methodology, Investigation, Funding acquisition, Formal analysis, Data curation, Conceptualization. **P. Valdivia:** Writing – review & editing, Investigation. **D. Bondar:** Writing – review & editing, Investigation. **S. Dominijanni:** Writing – review & editing, Investigation, Data curation. **S. Abeykoon:** Writing – review & editing, Investigation. **G. Giuliani:** Writing – review & editing, Investigation. **A. Kurnosov:** Writing – review & editing, Investigation. **G. Giordano:** Writing – review & editing, Writing – original draft. **M. Cassetta:** Writing – review & editing. **A. Vona:** Writing – review & editing. **C. Romano:** Writing – review & editing. **F. Arzilli:** Writing – review & editing, Writing – original draft, Validation, Supervision, Resources, Project administration, Investigation, Funding acquisition, Formal analysis, Conceptualization.

Declaration of competing interest

The authors declare that they have no known competing financial interests or personal relationships that could have appeared to influence the work reported in this paper.

Acknowledgments

D. Di Genova acknowledges the funding from the European Research Council (ERC) under the European Union's Horizon Europe research and innovation programme (NANO*V*OLC, ERC Consolidator Grant – No. 101044772). D. Di Genova acknowledges the Deutsche Forschungsgemeinschaft (DFG) project DI 2751/2–1. D. Di Genova and F. Arzilli acknowledge funding from the European Union's – Next Generation EU, Missione 4 Componente 1 CUP B53D23007230006. G. Giordano, C. Romano and A. Vona acknowledge the grant of Excellence Department of Science 2023-2027 (ROMA TRE University) provided by the Italian Ministry of Research (MUR). The authors thank R. Njul and S. Campagnola for sample preparation, and J. Deubener and A. Zandonà for insightful discussions on the results. M. Cinque is also thanked for support during the writing. The authors acknowledge the editor S. Calvari for handling our manuscript and the reviewers S. Kolzenburg and G. Iezzi for their valuable comments, which improved the quality of the manuscript.

Appendix A. Supplementary data

Supplementary data to this article can be found online at https://doi.org/10.1016/j.jvolgeores.2025.108276.

Data availability

All data is provided with the manuscript.

References

Adam, G., Gibbs, J.H., 1965. On the temperature dependence of cooperative relaxation properties in glass-forming liquids. J. Chem. Phys. 43, 139–146. https://doi.org/10.1063/1.1696442.

Allan, A.S.R., Morgan, D.J., Wilson, C.J.N., Millet, M.A., 2013. From mush to eruption in centuries: assembly of the super-sized Oruanui magma body. Contrib. Mineral. Petrol. 166, 143–164. https://doi.org/10.1007/s00410-013-0869-2.

Al-Mukadam, R., Di Genova, D., Bornhöft, H., Deubener, J., 2020. High rate calorimetry derived viscosity of oxide melts prone to crystallization. J. Non-Cryst. Solids 536.

Al-Mukadam, R., Zandonà, A., Deubener, J., 2021a. Kinetic fragility of pure TeO2 glass. J. Non-Cryst. Solids 554, 1–6. https://doi.org/10.1016/j.jnoncrysol.2020.120595.

Al-Mukadam, R., Götz, I.K., Stolpe, M., Deubener, J., 2021b. Viscosity of metallic glass-forming liquids based on Zr by fast-scanning calorimetry. Acta Mater. 221, 117370. https://doi.org/10.1016/j.actamat.2021.117370.

Ando, M.F., Benzine, O., Pan, Z., Garden, J.L., Wondraczek, K., Grimm, S., Schuster, K., Wondraczek, L., 2018. Boson peak, heterogeneity and intermediate-range order in binary SiO2-Al2O3 glasses. Sci. Rep. 8, 1–14. https://doi.org/10.1038/s41598-018-23574-1.

Angell, C.A., 1995. Formation of glasses from liquids and biopolymers. Science (80) 267, 1924–1935. https://doi.org/10.1126/science.267.5206.1924.

Arzilli, F., Polacci, M., La Spina, G., Le Deit, L., Llewellin, E.W.W., Brooker, R.A.R.A., Torres-Orozco, R., Di Genova, D., Neave, D.A., Hartley, M.E., Mader, H.M., Giordano, D., Atwood, R.C., Lee, P.D., Burton, M.R., Heidelbach, F., 2022. Dendritic crystallization in hydrous basaltic magmas controls magma mobility within the Earth's crust. Nat. Commun. 13. https://doi.org/10.1038/s41467-022-30890-8.

Bero, C.A., Plazek, D.J., 1991. Volume-dependent rate processes in an epoxy resin. J. Polym. Sci. Part B Polym. Phys. 29, 39–47. https://doi.org/10.1002/polb.1991.090290106.

Boari, E., Avanzinelli, R., Melluso, L., Giordano, G., Mattei, M., De Benedetti, A.A., Morra, V., Conticelli, S., 2009. Isotope geochemistry (Sr-Nd-Pb) and petrogenesis of leucite-bearing volcanic rocks from "Colli albani" volcano, roman magmatic province, Central Italy: Inferences on volcano evolution and magma genesis. Bull. Volcanol. 71, 977–1005. https://doi.org/10.1007/s00445-009-0278-6.

Bondar, D., Fei, H., Withers, A.C., Katsura, T., 2020. A rapid-quench technique for multi-anvil high-pressure-temperature experiments. Rev. Sci. Instrum. 91. https://doi.org/10.1063/5.0005936.

Bondar, D., Withers, A.C., Whittington, A.G., Fei, H., Katsura, T., 2023. Dissolution mechanisms of water in depolymerized silicate (peridotitic) glasses based on infrared spectroscopy. Geochim. Cosmochim. Acta 342, 45–61. https://doi.org/10.1016/j.gca.2022.11.029.

Bondar, D., Zandonà, A., Canizarès, A., Bilardello, D., Valdivia, P., Romano, C., Allix, M., Di Genova, D., 2025. Nanolite crystallization in volcanic glasses : insights from high - temperature raman spectroscopy and low - temperature rock - magnetic analysis. Geochem. Geophys. Geosyst. https://doi.org/10.1029/2024GC011846.

Bottinga, Y., Weill, D., 1972. The viscosity of magmatic silicate: a model for calculation. Am. J. Sci. 272 (5), 438–475. https://doi.org/10.2475/ajs.272.5.438.

Bouhifd, M.A., Whittington, A.G., Richet, P., 2001. Partial molar volume of water in phonolitic glasses and liquids. Contrib. Mineral. Petrol. 142, 235–243. https://doi.org/10.1007/s004100100286.

Bouhifd, M.A., Whittington, A.G., Roux, J., Richet, P., 2006. Effect of water on the heat capacity of polymerized aluminosilicate glasses and melts. Geochim. Cosmochim. Acta 70, 711–722. https://doi.org/10.1016/j.gca.2005.09.012.

Bouhifd, M.A., Whittington, A.G., Withers, A.C., Richet, P., 2013. Heat capacities of hydrous silicate glasses and liquids. Chem. Geol. 346, 125–134. https://doi.org/10.1016/j.chemgeo.2012.10.026.

Cáceres, F., Wadsworth, F.B., Scheu, B., Colombier, M., Madonna, C., Cimarelli, C., Hess, K.-U., Kaliwoda, M., Ruthensteiner, B., Dingwell, D.B., 2020. Can nanolites enhance eruption explosivity? Geology XX 1–5. https://doi.org/10.1130/G47317.1/5074194/g47317.pdf.

Cáceres, F., Scheu, B., Hess, K.-U., Cimarelli, C., Vasseur, J., Kaliwoda, M., Dingwell, D. B., 2021. From melt to crystals: the effects of cooling on Fe-Ti oxide nanolites crystallisation and melt polymerisation at oxidising conditions. Chem. Geol. 563. https://doi.org/10.1016/j.chemgeo.2021.120057.

Cáceres, F., Hess, K.-U., Eitel, M., Döblinger, M., McCartney, K.N., Colombier, M., Gilder, S.A., Scheu, B., Kaliwoda, M., Dingwell, D.B., 2024. Oxide nanolitisation-induced melt iron extraction causes viscosity jumps and enhanced explosivity in silicic magma. Nat. Commun. 15. https://doi.org/10.1038/s41467-024-44850-x.

Campagnola, S., Vona, A., Romano, C., Giordano, G., 2016. Crystallization kinetics and rheology of leucite-bearing tephriphonolite magmas from the Colli Albani volcano (Italy). Chem. Geol. 424, 12–29. https://doi.org/10.1016/j.chemgeo.2016.01.012.

Carrasco-Núñez, G., Bernal, J.P., Dávila, P., Jicha, B., Giordano, G., Hernández, J., 2018. Reappraisal of Los Humeros volcanic complex by new U/Th Zircon and 40Ar/39Ar Dating: implications for greater geothermal potential. Geochem. Geophys. Geosyst. 19, 132–149. https://doi.org/10.1002/2017GC007044.

Cashman, K.V., Giordano, G., 2014. Calderas and magma reservoirs. J. Volcanol. Geotherm. Res. 288, 28–45. https://doi.org/10.1016/j.jvolgeores.2014.09.007.

Cashman, K.V., Sparks, R.S.J., Blundy, J.D., 2017. Vertically extensive and unstable magmatic systems: a unified view of igneous processes. Science (80) 355, eaag3055. https://doi.org/10.1126/science.aag3055.

Cassetta, M., 2024. Medium-range structure modifications induced by Fe3+/Fetot. In volcanic glasses: a low-frequency Raman spectroscopy study. Eur. Phys. J. Plus 139. https://doi.org/10.1140/epjp/s13360-023-04838-w.

Cassetta, M., Di Genova, D., Zanatta, M., Ballaran, T.B., Kurnosov, A., Giarola, M., Mariotto, G., 2021. Estimating the viscosity of volcanic melts from the vibrational properties of their parental glasses. Sci. Rep. https://doi.org/10.1038/s41598-021-92407-5.

Cassetta, M., Vetere, F., Zanatta, M., Perugini, D., Alvaro, M., Giannetta, B., Zaccone, C., Daldosso, N., 2023a. Micro-Raman spectroscopy for a comprehensive understanding of the structural evolution of Basaltic-Andesite and Trachybasalt multiphase systems. Chem. Geol. 616, 121241. https://doi.org/10.1016/j.chemgeo.2022.121241.

Cassetta, M., Mariotto, G., Daldosso, N., De Bona, E., Biesuz, M., Sorarù, G.D., Almeev, R., Zanatta, M., Vetere, F., 2023b. Viscosity, boson peak and elastic moduli in the Na2O-SiO2 system. Minerals 13, 1–11. https://doi.org/10.3390/min13091166.

Cassetta, M., De Bona, E., Sambugaro, A., Enrichi, F., Daldosso, N., Giannetta, B., Zaccone, C., Biesuz, M., Sglavo, V.M., Almeev, R., Nodari, L., Giordano, D., Mariotto, G., 2025. Fe-dependent structural evolution of peralkaline soda aluminosilicate glasses: iron speciation vs. glass transition. Chem. Geol. 674, 122561. https://doi.org/10.1016/j.chemgeo.2024.122561.

Chevrel, M.O., Giordano, D., Potuzak, M., Courtial, P., Dingwell, D.B., 2013. Physical properties of CaAl2Si2O8-CaMgSi2O6-FeO-Fe2O3 melts: Analogues for extra-terrestrial basalt. Chem. Geol. 346, 93–105. https://doi.org/10.1016/j.chemgeo.2012.09.004.

Conticelli, S., Boari, E., Avanzinelli, R., De Benedetti, A.A., Giordano, G., Mattei, M., Melluso, L., Morra, V., 2010. Geochemistry, isotopes and mineral chemistry of the Colli Albani volcanic rocks: constraints on magma genesis and evolution. Colli Albani Volcano. https://doi.org/10.1144/IAVCEl003.6.

Delaney, P.T., Pollard, D.D., 1982. Solidification of basaltic magma in a dike. Am. J. Sci. 282, 856–885.

Di Fiore, F., Vona, A., Di Genova, D., Pontesilli, A., Calabrò, L., Mollo, S., Taddeucci, J., Romano, C., Scarlato, P., 2024. Magma titanium and iron contents dictate crystallization timescales and rheological behaviour in basaltic volcanic systems. Commun. Earth Environ. 5. https://doi.org/10.1038/s43247-024-01452-1.

Di Genova, D., Romano, C., Alletti, M., Misiti, V., Scarlato, P., 2014a. The effect of CO2 and H2O on Etna and Fondo Riccio (Phlegrean Fields) liquid viscosity, glass transition temperature and heat capacity. Chem. Geol. 377, 72–86. https://doi.org/10.1016/j.chemgeo.2014.04.001.

Di Genova, D., Romano, C., Giordano, D., Alletti, M., 2014b. Heat capacity, configurational heat capacity and fragility of hydrous magmas. Geochim. Cosmochim. Acta 142, 314–333. https://doi.org/10.1016/j.gca.2014.07.012.

Di Genova, D., Hess, K.-U., Chevrel, M.O., Dingwell, D.B., 2016. Models for the estimation of Fe3+/Fetot. Ratio in terrestrial and extra- terrestrial alkali- and iron-rich silicate glasses using Raman spectroscopy. Am. Mineral. 101, 943–952. https://doi.org/10.2138/am-2016-5534CCBYNCND.

Di Genova, D., Kolzenburg, S., Wiesmaier, S., Dallanave, E., Neuville, D.R., Hess, K.-U., Dingwell, D.B., 2017a. A chemical tipping point governing mobilization and eruption style of rhyolitic magma. Nature 552, 235–238. https://doi.org/10.1038/nature24488.

Di Genova, D., Sicola, S., Romano, C., Vona, A., Fanara, S., Spina, L., 2017b. Effect of iron and nanolites on Raman spectra of volcanic glasses: reassessment of existing strategies to estimate the water content. Chem. Geol. 475, 76–86. https://doi.org/10.1016/j.chemgeo.2017.10.035.

Di Genova, D., Caracciolo, A., Kolzenburg, S., 2018. Measuring the degree of “nanotilization” of volcanic glasses: understanding syn-eruptive processes recorded in melt inclusions. Lithos 318–319, 209–218. https://doi.org/10.1016/j.lithos.2018.08.011.

Di Genova, D., Zandonà, A., Deubener, J., 2020a. Unravelling the effect of nano-heterogeneity on the viscosity of silicate melts: implications for glass manufacturing and volcanic eruptions. J. Non-Cryst. Solids 545, 120248. https://doi.org/10.1016/j.jnoncrysol.2020.120248.

Di Genova, D., Brooker, R.A., Mader, H.M., Drewitt, J.W.E.E., Longo, A., Neuville, D.R., Fanara, S., Shebanova, O., Anzellini, S., Arzilli, F., Bamber, E.C., Hennet, L., Deubener, J., La Spina, G., Neuville, D.R., Fanara, S., Shebanova, O., Anzellini, S., Arzilli, F., Bamber, E.C., Hennet, L., La Spina, G., Miyajima, N., 2020b. In situ observation of nanolite growth in volcanic melt: a driving force for explosive eruptions. Sci. Adv. 6. https://doi.org/10.1126/sciadv.abb0413.

Di Genova, D., Bondar, D., Zandonà, A., Valdivia, P., Al-Mukadam, R., Fei, H., Withers, A. C., Boffa Ballaran, T., Kurnosov, A., McCammon, C.A., Deubener, J., Katsura, T., 2023. Viscosity of anhydrous and hydrous peridotite melts. Chem. Geol. 625. https://doi.org/10.1016/j.chemgeo.2023.121440.

Dingwell, D.B., 1996. Volcanic dilemma: flow or blow? Science (80) 273, 1054–1055. https://doi.org/10.1126/science.273.5278.1054.

Dingwell, D.B., Romano, C., Hess, K.-U., 1996. The effect of water on the viscosity of a haplogranitic melt under P-T-X conditions relevant to silicic volcanism. Contrib. Mineral. Petrol. 124, 19–28.

Dingwell, D.B., Hess, K.-U., Wilding, M., Brooker, R.A., Di Genova, D., Drewitt, J.W.E., Wilson, M., Weidendorfer, D., 2022. The glass transition and the non-Arrhenian viscosity of carbonate melts. Am. Mineral. 107, 1053–1064. https://doi.org/10.2138/am-2021-7752.

Douglas, R.W., Armstrong, W.L., Edward, J., Hall, D., 1965. A penetration viscometer. Glass Technol. 52–55.

Druitt, T.H., Costa, F., Deloule, E., Dungan, M., Scaillet, B., 2012. Decadal to monthly timescales of magma transfer and reservoir growth at a caldera volcano. Nature 482, 77–80.

First, E.C., Leonhardi, T.C., Hammer, J.E., 2020. Effects of superheating magnitude on olivine growth. Contrib. Mineral. Petrol. 175, 1–14. https://doi.org/10.1007/s00410-019-1638-7.

Freda, C., Gaeta, M., Giaccio, B., Marra, F., Palladino, D.M., Scarlato, P., Sottili, G., 2011. CO2-driven large mafic explosive eruptions: the Pozzolane Rosse case study from the Colli Albani Volcanic District (Italy). Bull. Volcanol. 73, 241–256. https://doi.org/10.1007/s00445-010-0406-3.

Giacomuzzi, G., Chiarabba, C., Bianco, F., De Gori, P., Agostinetti, N.P., 2024. Tracking transient changes in the plumbing system at Campi Flegrei Caldera. Earth Planet. Sci. Lett. 637, 118744. https://doi.org/10.1016/j.epsl.2024.118744.

Giordano, D., Russell, J.K., Dingwell, D.B., 2008a. Viscosity of magmatic liquids: a model. Earth Planet. Sci. Lett. 271, 123–134. https://doi.org/10.1016/j.epsl.2008.03.038.

Giordano, D., Potuzak, M., Romano, C., Dingwell, D.B., Nowak, M., 2008b. Viscosity and glass transition temperature of hydrous melts in the system CaAl2Si2O8-CaMgSi2O6. Chem. Geol. 256, 203–215. https://doi.org/10.1016/j.chemgeo.2008.06.027.

Giordano, D., Ardia, P., Romano, C., Dingwell, D.B., Di Muro, A., Schmidt, M.W., Mangiacapra, A., Hess, K.-U., 2009. The rheological evolution of alkaline Vesuvius magmas and comparison with alkaline series from the Phlegrean Fields, Etna, Stromboli and Teide. Geochim. Cosmochim. Acta 73, 6613–6630. https://doi.org/10.1016/j.gca.2009.07.033.

Giordano, D., Nichols, A.R.L.L., Potuzak, M., Di Genova, D., Romano, C., Russell, J.K., 2015. Heat capacity of hydrous trachybasalt from Mt Etna: comparison with CaAl2Si2O8 (An)–CaMgSi2O6 (Di) as basaltic proxy compositions. Contrib. Mineral. Petrol. 170, 48. https://doi.org/10.1007/s00410-015-1196-6.

Giordano, G., Caricchi, L., 2022. Determining the State of activity of Transcrustal Magmatic Systems and their Volcanoes. Annu. Rev. Earth Planet. Sci. 50, 231–259. https://doi.org/10.1146/annurev-earth-032320-084733.

Giordano, G., Team, T.C., 2010. Stratigraphy, volcano tectonics and evolution of the Colli Albani volcanic field. Colli Albani Volcano. https://doi.org/10.1144/IAVCEl003.4.

Giordano, G., De Benedetti, A.A., Diana, A., Diano, G., Gaudioso, F., Marasco, F., Miceli, M., Mollo, S., Cas, R., Funiciello, R., 2006. The Colli Albani mafic caldera (Roma, Italy): Stratigraphy, structure and petrology. J. Volcanol. Geotherm. Res. 155, 49–80. https://doi.org/10.1016/j.jvolgeores.2006.02.009.

Giuliani, G., Di Genova, D., Di, F., Valdivia, P., Mollo, S., Romano, C., Boffa, T., Kurnosov, A., Vona, A., 2024. The effect of carbonate assimilation and nanoheterogeneities on the viscosity of phonotephritic melt from Vesuvius. Chem. Geol. 670, 122408. https://doi.org/10.1016/j.chemgeo.2024.122408.

Gonnermann, H., Taisne, B., 2015. Chapter 10 - Magma transport in dikes. In: Sigurdsson, H. (Ed.), The Encyclopedia of Volcanoes, Second edition. Academic Press, Amsterdam, pp. 215–224. https://doi.org/10.1016/B978-0-12-385938-9.00010-9.

Gottsmann, J., Giordano, D., Dingwell, D.B., 2002. Predicting shear viscosity during volcanic processes at the glass transition: a calorimetric calibration. Earth Planet. Sci. Lett. 198, 417–427. https://doi.org/10.1016/S0012-821X(02)00522-8.

Gualda, G.A.R., Sutton, S.R., 2016. The year leading to a supereruption. PLoS One 11, 1–18. https://doi.org/10.1371/journal.pone.0159200.

Gualda, G.A.R., Pamukcu, A.S., Ghiorso, M.S., Anderson, A.T.J., Sutton, S.R., Rivers, M. L., 2012. Timescales of quartz crystallization and the longevity of the Bishop giant magma body. PLoS One 7, e37492. https://doi.org/10.1371/journal.pone.0037492.

Hess, K.-U., Dingwell, D.B., 1996. Viscosities of hydrous leucogranitic melts: a non-arrhenian model. Am. Mineral. 81, 1297–1300.

Hughes, E.C., Buse, B., Kearns, S.L., Blundy, J.D., Mader, H.M., Carlo, M., 2019. Low analytical totals in EPMA of hydrous silicate glass due to sub-surface charging: Obtaining accurate volatiles by difference, 505, 48–56. https://doi.org/10.1016/j.chemgeo.2018.11.015.

Hui, H., Zhang, Y., 2007. Toward a general viscosity equation for natural anhydrous and hydrous silicate melts. Geochim. Cosmochim. Acta 71, 403–416. https://doi.org/10.1016/j.gca.2006.09.003.

Iacovino, K., Till, C.B., 2019. DensityX: a program for calculating the densities of magmatic liquids up to 1,627 °C and 30 kbar. Volcanica 2, 1–10. https://doi.org/10.30909/vol.02.01.0110.

Jorgenson, C., Caricchi, L., Chiaradia, M., Ágreda-López, M., Giordano, G., 2024. Rapid accumulation and ascent precedes caldera forming eruption of low viscosity magma. Contrib. Mineral. Petrol. 179, 1–19. https://doi.org/10.1007/s00410-023-02091-z.

Karner, D.B., Marra, F., Renne, P.R., 2001. The history of the Monti Sabatini and Alban Hills volcanoes: ground for assessing volcanic-tectonic hazards for Rome. J. Volcanol. Geotherm. Res. 107, 185–219. https://doi.org/10.1016/S0377-0273(00)00258-4.

Kleest, C., Webb, S.L., 2022. Influence of Fe2+/Fetot on the viscosity of melts from the Colli Albani Volcanic District (Italy) – foidite to phonolite. J. Volcanol. Geotherm. Res. 431, 107649. https://doi.org/10.1016/j.jvolgeores.2022.107649.

Kleest, C., Webb, S.L., Fanara, S., 2020. Rheology of melts from the colli albani volcanic district (Italy): a case study. Contrib. Mineral. Petrol. 175. https://doi.org/10.1007/s00410-020-01720-1.

Knafelc, J., Bryan, S.E., Jones, M.W.M., Gust, D., Mallmann, G., Cathey, H.E., Berry, A.J., Ferré, E.C., Howard, D.L., 2022. Havre 2012 pink pumice is evidence of a short-lived, deep-sea, magnetite nanolite-driven explosive eruption. Commun. Earth Environ. 3, 1–11. https://doi.org/10.1038/s43247-022-00355-3.

Kohl, I., Bachmann, L., Mayer, E., Hallbrucker, A., Loerting, T., 2005. Glass transition in hyperquenched water? Nature 435, E1. https://doi.org/10.1038/nature03707.

Kolzenburg, S., Chevrel, M.O., Dingwell, D.B., 2022. Magma/Suspension Rheology. Rev. Mineral. Geochem. 87, 639–720. https://doi.org/10.2138/rmg.2022.87.14.

La Spina, G., Burton, M.R., de Michieli Vitturi, M., Arzilli, F., 2016. Role of syn-eruptive plagioclase disequilibrium crystallization in basaltic magma ascent dynamics. Nat. Commun. 7, 13402. https://doi.org/10.1038/ncomms13402.

La Spina, G., Arzilli, F., Llewellin, E.W., Burton, M.R., Clarke, A.B., de Michieli Vitturi, M., Polacci, M., Hartley, M.E., Di Genova, D., Mader, H.M., 2021. Explosivity of basaltic lava fountains is controlled by magma rheology, ascent rate and outgassing. Earth Planet. Sci. Lett. 1, 116658. https://doi.org/10.1016/j.epsl.2020.116658.

Langhammer, D., Di Genova, D., Steinle-Neumann, G., 2021. Modelling the viscosity of anhydrous and hydrous volcanic melt. Geochem. Geophys. Geosyst., e2021GC009918 https://doi.org/10.1029/2021GC009918.

Langhammer, D., Di Genova, D., Steinle-Neumann, G., 2022. Modelling viscosity of volcanic melts with artificial neural networks. Geochem. Geophys. Geosyst. 23. https://doi.org/10.1029/2022GC010673.

Le Losq, C., Neuville, D.R., Chen, W., Florian, P., Massiot, D., Zhou, Z., Greaves, G.N., 2017. Percolation channels: a universal idea to describe the atomic structure and dynamics of glasses and melts. Sci. Rep. 7, 1–12. https://doi.org/10.1038/s41598-017-16741-3.

Le Losq, C., Berry, A.J., Kendrick, M.A., Neuville, D.R., O'Neill, H.S.C., 2019. Determination of the oxidation state of iron in Mid-Ocean Ridge basalt glasses by Raman spectroscopy. Am. Mineral. 104, 1032–1042. https://doi.org/10.2138/am-2019-6887.

Le Mével, H., Feigl, K.L., Cõrdova, L., DeMets, C., Lundgren, P., 2015. Evolution of unrest at Laguna del Maule volcanic field (Chile) from InSAR and GPS measurements, 2003 to 2014. Geophys. Res. Lett. 42, 6590–6598. https://doi.org/10.1002/2015GL064665.

Liebske, C., Behrens, H., Holtz, F., Lange, R.A., 2003. The influence of pressure and composition on the viscocity of andesitic melts. Geochim. Cosmochim. Acta 67, 473–485. https://doi.org/10.1016/S0016-7037(02)01139-0.

Lister, J.R., Kerr, R.C., 1991. Fluid-mechanical models of crack propagation and their application to magma transport in dykes. J. Geophys. Res. 96, 10,049–10,077.

Marsh, B.D., Kantha, L.H., 1978. On the heat and mass transfer from an ascending magma. Earth Planet. Sci. Lett. 39, 435–443. https://doi.org/10.1016/0012-821X(78)90032-8.

Marxer, H., Bellucci, P., Nowak, M., 2015. Degassing of H_2O in a phonolitic melt: a closer look at decompression experiments. J. Volcanol. Geotherm. Res. 297, 109–124. https://doi.org/10.1016/j.jvolgeores.2014.11.017.

Mauro, J.C., Yue, Y.Z., Ellison, A.J., Gupta, P.K., Allan, D.C., 2009. Viscosity of glass-forming liquids. Proc. Natl. Acad. Sci. USA 106, 19780–19784. https://doi.org/10.1073/pnas.0911705106.

Meerlender, G., 1974. Viskositäts-temperaturverhalten des standardglases I der DGG. Glas. Ber. 47, 1–3.

Moynihan, C.T., 1995. Structural relaxation and the glass transition. Rev. Mineral. 32, 1–19.

Mujin, M., Nakamura, M., 2014. A nanolite record of eruption style transition. Geology 42, 611–614. https://doi.org/10.1130/G35553.1.

Mujin, M., Nakamura, M., 2020. Late-stage groundmass differentiation as a record of magma stagnation, fragmentation, and rewelding. Bull. Volcanol. 82.

Mujin, M., Nakamura, M., Miyake, A., 2017. Eruption style and crystal size distributions: Crystallization of groundmass nanolites in the 2011 Shinmoedake eruption. Am. Mineral. 102, 2367–2380. https://doi.org/10.1186/s12986.

Mysen, B.O., Virgo, D., 1986. Volatiles in silicate melts at high pressure and temperature. Chem. Geol. 57, 333–358. https://doi.org/10.1016/0009-2541(86)90057-4.

Mysen, B.O., Virgo, D., Scarfe, C.M., 1980. Relations between anionic structure and viscosity of silicate melts - a Raman spectroscopic study. Am. Mineral. 65, 690–710.

Mysen, B.O., Virgo, D., Seifert, F.A., 1985. Relationships between properties and structure of aluminosilicate melts. Am. Mineral. 70, 88–105.

Narayanaswamy, O.S., 1971. A model of structural relaxation in glass. J. Am. Ceram. Soc. 54, 491–498. https://doi.org/10.1111/j.1151-2916.1971.tb12186.x.

Novikov, V.N., Sokolov, A.P., 2004. Poisson's ratio and the fragility of glass-forming liquids. Nature 431, 961–963. https://doi.org/10.1038/nature02947.

Ohlhorst, S., Behrens, H., Holtz, F., 2001. Compositional dependence of molar absorptivities of near-infrared OH- and H_2O bands in rhyolitic to basaltic glasses. Chem. Geol. 174, 5–20. https://doi.org/10.1016/S0009-2541(00)00303-X.

Okumura, S., Uesugi, K., Goto, A., Takeuchi, A., Miyake, A., 2022a. Rheology of nanocrystal-bearing andesite magma and its roles in explosive volcanism. Commun. Earth Environ. 3, 1–7. https://doi.org/10.1038/s43247-022-00573-9.

Okumura, S., Mujin, M., Tsuchiyama, A., Miyake, A., 2022b. 3D crystal size distributions of pyroxene nanolites from nano X-ray computed tomography: improved correction of crystal size distributions from CSDCorrections for magma ascent dynamics in conduits. Am. Mineral. 107, 1766–1778. https://doi.org/10.2138/am-2022-8039.

Okumura, S., Mujin, M., Tsuchiyama, A., Miyake, A., 2023. Crystal habit (tracht) of groundmass pyroxene crystals recorded magma ascent paths during the 2011 Shinmoedake eruption. Am. Mineral. 109, 325–338. https://doi.org/10.2138/am-2022-8765.

Palladino, D.M., Gaeta, M., Marra, F., 2001. A large K-foiditic hydromagmatic eruption from the early activity of the Alban Hills Volcanic District, Italy. Bull. Volcanol. 63, 345–359. https://doi.org/10.1007/s004450100150.

Pamukcu, A.S., Gualda, G.A.R., Bégué, F., Gravley, D.M., 2015. Melt inclusion shapes: Timekeepers of short-lived giant magma bodies. Geology 43, 947–950. https://doi.org/10.1130/G37021.1.

Pereira, L., Linard, Y., Wadsworth, F.B., Vasseur, J., Hess, K.-U., Moretti, R., Dingwell, D.B., Neuville, D.R., 2024. The rheological response of magma to nanolitisation. J. Volcanol. Geotherm. Res. 448. https://doi.org/10.1016/j.jvolgeores.2024.108039.

Prescher, C., McCammon, C.A., Dubrovinsky, L., 2012. MossA: a program for analyzing energy-domain Mössbauer spectra from conventional and synchrotron sources. J. Appl. Crystallogr. 45, 329–331. https://doi.org/10.1107/S0021889812004979.

Richet, P., Lejeune, A.M., Holtz, F., Roux, J., 1996. Water and the viscosity of andesite melts. Chem. Geol. 128, 185–197. https://doi.org/10.1016/0009-2541(95)00172-7.

Richet, P., Whittington, A.G., Holtz, F., Behrens, H., Ohlhorst, S., Wilke, M., 2000. Water and the density of silicate glasses. Contrib. Mineral. Petrol. 138, 337–347. https://doi.org/10.1007/s004100050567.

Robert, G., Knipping, J.L., Scherbarth, S., Robertson, T.E., Stechern, A.A., Behrens, H., Whittington, A.G., 2014a. Heat capacity and viscosity of basaltic melts with H_2O ± F ± CO_2. Chem. Geol. https://doi.org/10.1016/j.chemgeo.2014.07.015.

Robert, G., Whittington, A.G., Stechern, A., Behrens, H., 2014b. Heat capacity of hydrous basaltic glasses and liquids. J. Non-Cryst. Solids 390, 19–30. https://doi.org/10.1016/j.jnoncrysol.2014.02.011.

Romano, C., Poe, B.T., Mincione, V., Hess, K.-U., Dingwell, D.B., 2001. The viscosities of dry and hydrous $XAlSi_3O_8$ (X = Li, Na, K, Ca-0.5, Mg-0.5) melts. Chem. Geol. 174, 115–132. ST-The viscosities of dry and hydrous X.

Romine, W.L., Whittington, A.G., 2015. A simple model for the viscosity of rhyolites as a function of temperature, pressure and water content. Geochim. Cosmochim. Acta 170, 281–300. https://doi.org/10.1016/j.gca.2015.08.009.

Scarani, A., Zandonà, A., Di Fiore, F., Valdivia, P., Putra, R., Miyajima, N., Bornhöft, H., Vona, A., Deubener, J., Romano, C., Di Genova, D., 2022a. A chemical threshold controls nanocrystallization and degassing behaviour in basalt magmas. Commun. Earth Environ. 3. https://doi.org/10.1038/s43247-022-00615-2.

Scarani, A., Vona, A., Di Genova, D., Al-Mukadam, R., Romano, C., Deubener, J., 2022b. Determination of cooling rates of glasses over four orders of magnitude. Contrib. Mineral. Petrol. 177, 1–17. https://doi.org/10.1007/s00410-022-01899-5.

Schawe, J.E.K., Hess, K.-U., 2019. The kinetics of the glass transition of silicate glass measured by fast scanning calorimetry. Thermochim. Acta 677, 85–90. https://doi.org/10.1016/j.tca.2019.01.001.

Scherer, G.W., 1984. Use of the Adam-Gibbs equation in the analysis of structural relaxation. J. Am. Ceram. Soc. 67, 504–511.

Schneider, H.A., Rieger, J., Penzel, E., 1997. The glass transition temperature of random copolymers: 2. Extension of the Gordon - Taylor equation for asymmetric Tg vs composition curves. Polymer (Guildf). 38, 1323–1337. https://doi.org/10.1016/S0032-3861(96)00652-0.

Scopigno, T., Ruocco, G., Sette, F., Monaco, G., 2003. Is the fragility of a liquid embedded in the Properties of its Glass? Science (80) 302, 849–852. https://doi.org/10.1126/science.1089446.

Sehlke, A., Whittington, A.G., Robert, B., Harris, A., Gurioli, L., Médard, E., 2014. Pahoehoe to áá transition of Hawaiian lavas: an experimental study. Bull. Volcanol. 76. https://doi.org/10.1007/s00445-014-0876-9.

Seifert, R., Malfait, W.J., Petitgirard, S., Sanchez-Valle, C., 2013. Density of phonolitic magmas and time scales of crystal fractionation in magma chambers. Earth Planet. Sci. Lett. 381, 12–20. https://doi.org/10.1016/j.epsl.2013.08.039.

Shamloo, H.I., Till, C.B., 2019. Decadal transition from quiescence to supereruption: petrologic investigation of the Lava Creek Tuff, Yellowstone Calder, WY. Contrib. Mineral. Petrol. 174, 1–18. https://doi.org/10.1007/s00410-019-1570-x.

Shaw, H.R., 1972. Viscosities of magmatic silicate liquids: an empirical method of prediction. Am. J. Sci. 272, 870–893.

Shuker, R., Gammon, R.W., 1970. Raman-scattering selection-rule breaking and the density of states in amorphous materials. Phys. Rev. Lett. 25, 222–225. https://doi.org/10.1103/PhysRevLett.25.222.

Sipp, A., Richet, P., 2002. Equivalence of volume, enthalpy and viscosity relaxation kinetics in glass-forming silicate liquids. J. Non-Cryst. Solids 298, 202–212. https://doi.org/10.1016/S0022-3093(02)00948-1.

Stabile, P., Sicola, S., Giuli, G., Paris, E., Carroll, M.R., Deubener, J., Di Genova, D., 2021. The effect of iron and alkali on the nanocrystal-free viscosity of volcanic melts: a combined Raman spectroscopy and DSC study. Chem. Geol. 559, 119991. https://doi.org/10.1016/j.chemgeo.2020.119991.

Stebbins, J.F., Carmichael, I.S.E., Moret, L.K., 1984. Heat capacities and entropies of silicate liquids and glasses. Contrib. Mineral. Petrol. 86, 131–148. https://doi.org/10.1007/BF00381840.

Stevenson, R.J., Dingwell, D.B., Webb, S.L., Bagdassarov, N.S., 1995. The equivalence of enthalpy and shear stress relaxation in rhyolitic obsidians and quantification of the liquid-glass transition in volcanic processes. J. Volcanol. Geotherm. Res. 68, 297–306. https://doi.org/10.1016/0377-0273(95)00015-1.

Stevenson, R.J., Bagdassarov, N.S., Romano, C., 1997. Vesiculation processes in a water-rich calc-alkaline obsidian. Earth Planet. Sci. Lett. 146, 555–571.

Stevenson, R.J., Dingwell, D.B., Bagdassarov, N.S., Manley, C.R., 2001. Measurement and implication of "effective" viscosity for rhyolite flow emplacement. Bull. Volcanol. 63, 227–237. https://doi.org/10.1007/s004450100137.

Toplis, M.J., Gottsmann, J., Knoche, R., Dingwell, D.B., 2001. Heat capacities of haplogranitic glasses and liquids. Geochim. Cosmochim. Acta 65, 1985–1994.

Trubowitz, C., Murakami, M., Petitgirard, S., Liebske, C., McCammon, C., 2024. Structural evolution of basaltic melts in the deep earth: insights from high-pressure sound velocity of glass. J. Geophys. Res. Solid Earth 129. https://doi.org/10.1029/2024JB028969.

Valdivia, P., Zandonà, A., Kurnosov, A., Ballaran, T.B., Deubener, J., Di Genova, D., 2023. Are volcanic melts less viscous than we thought? The case of Stromboli basalt. Contrib. Mineral. Petrol. 178.

Valdivia, P., Zandonà, A., Löschmann, J., Bondar, D., Genevois, C., Allix, M., Miyajima, N., Kurnosov, A., Boffa Ballaran, T., Di Fiore, F., Vona, A., Romano, C., Deubener, J., Bamber, E.C., Di Genova, D., 2024. Nanoscale chemical heterogeneities control magma viscosity and failure. Under Rev. 1–25. https://doi.org/10.21203/rs.3.rs-3891365/v1.

Velikov, V., Borick, S., Angell, C.A., 2001. The glass transition of water, based on Hyperquenching experiments. Science (80) 294, 2335–2338. https://doi.org/10.1126/science.1061757.

Verdurme, P., Le Losq, C., Chevrel, O., Pannefieu, S., Médard, E., Berthod, C., Komorowski, J.C., Bachèlery, P., Neuville, D.R., Gurioli, L., 2023. Viscosity of crystal-free silicate melts from the active submarine volcanic chain of Mayotte. Chem. Geol. 620. https://doi.org/10.1016/j.chemgeo.2023.121326.

Vetere, F., Behrens, H., Misiti, V., Ventura, G., Holtz, F., De Rosa, R., Deubener, J., 2007. The viscosity of shoshonitic melts (Vulcanello Peninsula, Aeolian Islands, Italy): Insight on the magma ascent in dikes. Chem. Geol. 245, 89–102. https://doi.org/10.1016/j.chemgeo.2007.08.002.

Vetere, F., Iezzi, G., Behrens, H., Cavallo, A., Misiti, V., Dietrich, M., Knipping, J., Ventura, G., Mollo, S., 2013. Intrinsic solidification behaviour of basaltic to rhyolitic melts: a cooling rate experimental study. Chem. Geol. 354, 233–242. https://doi.org/10.1016/j.chemgeo.2013.06.007.

Vetere, F., Iezzi, G., Behrens, H., Holtz, F., Ventura, G., Misiti, V., Cavallo, A., Mollo, S., Dietrich, M., 2015. Glass forming ability and crystallisation behaviour of sub-alkaline silicate melts. Earth-Sci. Rev. 150, 25–44. https://doi.org/10.1016/j.earscirev.2015.07.001.

Vinkler, A.P., Cashman, K.V., Giordano, G., Groppelli, G., 2012. Evolution of the mafic Villa Senni caldera-forming eruption at Colli Albani volcano, Italy, indicated by textural analysis of juvenile fragments. J. Volcanol. Geotherm. Res. 235–236, 37–54. https://doi.org/10.1016/j.jvolgeores.2012.03.006.

Wadsworth, F.B., Vasseur, J., Lavallée, Y., Hess, K.-U., Kendrick, J.E., Castro, J.M., Weidendorfer, D., Rooyakkers, S.M., Foster, A., Jackson, L.E., Kennedy, B.M., Nichols, A.R.L., Schipper, C.I., Scheu, B., Dingwell, D.B., Watson, T., Rule, G., Witcher, T., Tuffen, H., 2024. The rheology of rhyolite magma from the IDDP-1 borehole and Hrafntinnuhryggur (Krafla, Iceland) with implications for geothermal drilling. J. Volcanol. Geotherm. Res. 455. https://doi.org/10.1016/j.jvolgeores.2024.108159.

Webb, S.L., Knoche, R., 1996. The glass-transition, structural relaxation and shear viscosity of silicate melts. Chem. Geol. 128, 165–183. https://doi.org/10.1016/0009-2541(95)00171-9.

Whitfield, C.H., Brody, E.M., Bassett, W., 1976. Elastic moduli of NaCl by Brillouin scattering at high pressure in a diamond anvil cell. Rev. Sci. Instrum. 47, 942–947.

Whittington, A.G., Richet, P., Linard, Y., Holtz, F., 2001a. The viscosity of hydrous phonolites and trachytes. Chem. Geol. https://doi.org/10.1016/S0009-2541(00)00317-X.

Whittington, A.G., Richet, P., Linard, Y., Holtz, F., 2001b. The viscosity of hydrous phonolites and trachytes. Chem. Geol. 174, 209–223. https://doi.org/10.1016/S0009-2541(00)00317-X.

Wiebe, R.A., Kolzenburg, S., Rooyakkers, S.M., Stix, J., 2021. Plutonic record of a caldera-forming silicic eruption: the shatter zone of the Cadillac Mountain granite, coastal Maine. Geosphere 17, 1–22. https://doi.org/10.1130/GES02252.1.

Wilding, M., Webb, S.L., Dingwell, D.B., 1995. Evaluation of a relaxation geospeedometer for volcanic glasses. Chem. Geol. 125, 137–148.

Wotzlaw, J.F., Bindeman, I.N., Stern, R.A., D`Abzac, F.X., Schaltegger, U., 2015. Rapid heterogeneous assembly of multiple magma reservoirs prior to Yellowstone supereruptions. Sci. Rep. 5, 1–10. https://doi.org/10.1038/srep14026.

Yoshida, K., Tamura, Y., Sato, T., Hanyu, T., Usui, Y., Chang, Q., Ono, S., 2022. Variety of the drift pumice clasts from the 2021 Fukutoku-Oka-no-Ba eruption, Japan. Island Arc 1–17. https://doi.org/10.1111/iar.12441.

Yue, Y.Z., 2008. Characteristic temperatures of enthalpy relaxation in glass. J. Non-Cryst. Solids 354, 1112–1118. https://doi.org/10.1016/j.jnoncrysol.2006.11.027.

Yue, Y.Z., Christiansen, J. de C., Jensen, S.L., 2002. Determination of the fictive temperature for a hyperquenched glass. Chem. Phys. Lett. 357, 20–24. https://doi.org/10.1016/S0009-2614(02)00434-7.

Yue, Y.Z., Von der Ohe, R., Jensen, S.L., 2004. Fictive temperature, cooling rate, and viscosity of glasses. J. Chem. Phys. 120, 8053–8059. https://doi.org/10.1063/1.1689951.

Zandonà, A., Rüdinger, B., Hochrein, O., Deubener, J., 2019a. Crystallization sequence within the keatite solid solution – cordierite mixed compositional triangle with TiO2 as nucleating agent. J. Non-Cryst. Solids 505, 320–332. https://doi.org/10.1016/j.jnoncrysol.2018.11.012.

Zandonà, A., Patzig, C., Rüdinger, B., Hochrein, O., Deubener, J., 2019b. TiO2(B) nanocrystals in Ti-doped lithium aluminosilicate glasses. J. Non-Crystalline Solids X 2, 100025. https://doi.org/10.1016/j.nocx.2019.100025.

Zandonà, A., Moustrous, M., Genevois, C., Véron, E., Canizarès, A., Allix, M., 2022a. Glass-forming ability and ZrO2 saturation limits in the magnesium aluminosilicate system. Ceram. Int. 48, 8433–8439. https://doi.org/10.1016/j.ceramint.2021.12.051.

Zandonà, A., Ory, S., Genevois, C., Véron, E., Canizarès, A., Pitcher, M.J., Allix, M., 2022b. Glass formation and devitrification behavior of alkali (Li, Na) aluminosilicate melts containing TiO2. J. Non-Cryst. Solids 582, 121448. https://doi.org/10.1016/j.jnoncrysol.2022.121448.

Zandonà, A., Scarani, A., Jessica, L., Di Fiore, F., de Ligny, D., Deubener, J., Vona, A., Allix, M., Di Genova, D., 2023. Non-stoichiometric crystal nucleation in a spodumene glass containing TiO2 as seed former: Effects on the viscosity of the residual melt. J. Non-Cryst. Solids 619. https://doi.org/10.1016/j.jnoncrysol.2023.122563.

Zhang, Y., Xu, Z., Liu, Y., 2003. Viscosity of hydrous rhyolitic melts inferred from kinetic experiments, and a new viscosity model. Am. Mineral. 88, 1741–1752. https://doi.org/10.2138/am-2003-11-1215.

Zheng, Q.J., Mauro, J.C., Yue, Y.Z., 2017. Reconciling calorimetric and kinetic fragilities of glass-forming liquids. J. Non-Cryst. Solids 456, 95–100. https://doi.org/10.1016/j.jnoncrysol.2016.11.014.